

EarthArXiv Coversheet

April 1, 2022

**The effects of a weak asthenospheric layer on surface kinematics,
subduction dynamics and slab morphology in the lower mantle**

This manuscript is **non-peer reviewed preprint** submitted to *Journal of Geophysical Research : Solid Earth* and thus may be periodically revised. The final version will be available via the 'Peer-review Publication DOI' link on the right-hand side of this webpage.

Please feel free to contact the corresponding author; we welcome feedback.

Earth  ArXiv

1 The effect of a weak asthenospheric layer on surface
2 kinematics, subduction dynamics and slab
3 morphology in the lower mantle

4 Nestor G. Cerpa¹, Karin Sigloch², Fanny Garel¹, Arnaud Heuret³, D.
5 Rhodri Davies⁴, and Mitchell G. Mihalynuk⁵

6 ¹*Geosciences Montpellier, Université de Montpellier, CNRS, Université des Antilles, Place Eugène Bataillon,*
7 *34095 Montpellier, France*

8 ²*Geoazur, Université Côte d'Azur, CNRS, Observatoire de la Côte d'Azur, IRD, 250 Avenue Albert Einstein,*
9 *06560 Valbonne, France*

10 ³*Université de Guyane, Géosciences Montpellier, 97300, Cayenne, France*

11 ⁴*Research School of Earth Sciences, The Australian National University, Canberra, ACT, 2601, Australia*

12 ⁵*British Columbia Geological Survey, PO Box 9333 Stn Prov Govt, Victoria, British Columbia V8W 9N3,*
13 *Canada*

14
15 **Abstract**

16 On Earth, the velocity at which subducting plates are consumed at their trenches (termed
17 ‘subduction rate’ herein) is typically 3 times higher than trench migration velocities. The
18 subduction rate is also 5 times higher than estimated lower mantle slab sinking rates. Us-
19 ing simple kinematic analyses, we show that if this present-day “kinematic state” operated
20 into the past, the subducting lithosphere should have accumulated and folded beneath
21 near-stationary trenches. These predictions are consistent with seismic tomography, which
22 images localized and widened lower-mantle slab piles. They are, however, at odds with
23 most dynamic-subduction models, which predict rapid trench retreat and inclined slabs
24 in the mantle transition zone. We test the hypothesis that a weak asthenospheric layer
25 (WAL), between the lithosphere-asthenosphere boundary and 220 km depth, compatible
26 with geophysical constraints, can remedy the discrepancies between numerical models and
27 observations. The WAL lubricates the base of the lithosphere, increases the subduction
28 rate while reducing trench retreat. As a consequence, simulations featuring a WAL pre-
29 dict slab accumulation at the mantle transition zone, and thicker, folded slabs in the
30 lower mantle. A WAL viscosity only 2-5 times lower than that of the adjacent mantle is
31 sufficient to shift subduction regimes towards a mode of vertical slab sinking and folding
32 beneath near-stationary trenches, across a wide range of model parameters, producing
33 surface and slab velocities close to those observed at the present-day. These findings
34 provide support for the existence of a weak asthenosphere beneath Earth’s lithosphere,
35 complementing independent evidence from various geophysical data.

1 Introduction

The negative buoyancy of subducting plates is the primary driving force sustaining subduction and surface plate motions Forsyth & Uyeda (1975). Subduction zones are the sites of tectonically-forced horizontal deformation Uyeda & Kanamori (1979); Lallemand et al. (2005) and dynamic vertical motions Davies (1981); Gurnis (1993). Crust and lithosphere subducting beyond the mantle transition zone add chemical heterogeneities to the lower mantle, which are stirred and homogenised by mantle convection Zindler & Hart (1986); Jones et al. (2016), or persist to the core-mantle-boundary, as suggested by modern tomographic models (e.g. Hosseini et al., 2020). Understanding the deep dynamics of subducting slabs is thus key for addressing the geodynamical and geochemical evolution of our planet.

Observed plate kinematics provide insights into the dynamics of the subduction system Forsyth & Uyeda (1975); Jarrard (1986); Lallemand et al. (2005); Heuret & Lallemand (2005); Sdrolias & Müller (2006); Doglioni et al. (2007); Funicello et al. (2008); Schellart (2008b); Becker & Faccenna (2009); Goes et al. (2011). Subduction kinematics (see Fig. 1) involve the velocities of the subducting plate v_{sp} ("SP velocity" for short); the velocity of the overriding plate v_{op} ("OP velocity"); and the velocity of the trench v_t , which is equal to OP velocity if the overriding plate does not undergo (back-arc) deformation. Note that v_{sp} and v_t are defined with opposite signs: the natural (positive) direction of trench migration is "retreat" towards the SP. These velocities are given in some absolute reference frame, which is taken as the stable lower mantle herein Becker & Faccenna (2009).

We also use a relative velocity, the subduction rate v_s . This is the velocity of the subducting plate relative to the trench (i. e., the rate at which the subducting plate is consumed by the migrating trench). It has been repeatedly shown that typical values of v_s on Earth are higher than 3-4 cm/yr Forsyth & Uyeda (1975); Jarrard (1986), while absolute trench motions are usually between -2 and 2 cm/yr Heuret & Lallemand (2005); Funicello et al. (2008); Schellart (2008b). Other studies have pointed out that the magnitude of the (absolute) SP velocity v_{sp} is generally two to three times higher than that of the (absolute) v_t Becker & Faccenna (2009); Goes et al. (2011); Carluccio et al. (2019). Hence plates are consumed at much faster rates than their trenches move laterally.

Analogue and numerical models of subduction dynamics without external forcing (hereafter simply referred to as models of subduction dynamics) have shed light on the internal force balance of subduction systems and the resulting kinematics. They have illuminated various subduction regimes and slab morphologies in the upper mantle (e. g. Guillou-Frottier et al., 1995; Schellart, 2008a; Di Giuseppe et al., 2008; Ribe, 2010; Stegman et al., 2010). Recent studies that included an overriding plate with finite strength, concluded that the slab pull force associated with the negative buoyancy of a subducting plate (SP) favored slab rollback and migration of of the trench towards the subducting plate (i. e., trench retreat), unless the SP was weak and/or the overriding plate (OP) was strong Garel et al. (2014); Sharples et al. (2014); Holt et al. (2015); Hertgen et al. (2020). It has been pointed out that such analogue and numerical models of subduction dynamics tend to produce surface kinematics that are at odds with some of the first-order observations outlined above Goes et al. (2011); Carluccio et al. (2019). These subduction models generally produce trench retreat velocities that exceed present-day observations, especially once the subducting slab reaches the bottom of the upper mantle, which was sometimes treated as a rigid barrier Funicello et al. (2004); Schellart (2005);

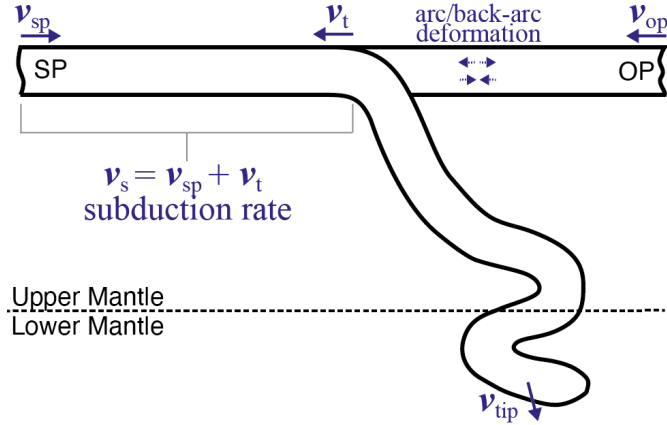


Figure 1: a) Sketch illustrating the various kinematics that can be inferred within a subduction system. Positive values denote absolute trenchward motion for both the subducting plate (p) and the overriding plate (v_{op}). Absolute trench velocity (v_t) is considered positive towards the subducting plate. We define relative to a fixed lower-mantle reference frame, in order to compare to absolute motions in nature, which can be quantified in empirical, approximate mantle reference frames, such as the fixed-hotspot frame. Subduction velocity (v_s) is a relative velocity, the rate at which the subducting plate is consumed at the trench ($v_s = v_{sp} + v_t$).

83 Capitanio et al. (2007); Goes et al. (2011). More modest trench motions over a relatively
 84 wide range of parameters have only been produced by 2-D models that consider both the
 85 penetration of the subducting slab into the lower mantle and complex rheologies Garel
 86 et al. (2014); Holt et al. (2015); Li et al. (2019). Even then, slower trench motion is only
 87 achieved at the cost of decreasing the SP velocity to values of less than 2 cm/yr once the
 88 slab interacts with the viscosity increase around 660-km depth (hereafter referred to as
 89 “first slab-660 interaction”) (e.g. Garel et al., 2014; Suchoy et al., 2021). Hence, in most
 90 subduction dynamics models, more than half of the subduction rate v_{sp} is accounted for
 91 by trench motion v_t , which contradicts present-day observations of plate kinematics.

92 Independent constraints on subduction dynamics come from seismic tomographic im-
 93 ages of slab morphologies at and below the mantle transition zone. A few slabs under
 94 present-day subduction zones in the Western Pacific appear to stagnate above the 660-km
 95 discontinuity Karason & Van Der Hilst (2000); Amaru (2007); Li et al. (2008); Fukao &
 96 Obayashi (2013) - for instance, under Japan Fukao et al. (1992) and under Izu-Bonin Wu
 97 et al. (2016), at least under its northernmost part Zhang et al. (2019). But many other
 98 slabs have breached the 660-km discontinuity and are sinking into the lower mantle Goes
 99 et al. (2017). Transition-zone and lower-mantle slabs are imaged more robustly and con-
 100 sistently than slabs in the upper(most) mantle. The opposite would be expected if slabs
 101 retained a constant thickness across depths. Hence the deeper slab must be thicker Ribe
 102 et al. (2007); Loiselet et al. (2010), which is well-documented under the Americas Karason
 103 & Van Der Hilst (2000); Ren et al. (2007); Sigloch & Mihalynuk (2013); Mohammadzaheri
 104 et al. (2021), but also globally Van der Voo et al. (1999); Shephard et al. (2017); Van der
 105 Meer et al. (2018); Hosseini et al. (2020). Under the particularly well-instrumented Cas-
 106 cadia subduction zone of North America, tomography can resolve a shallow slab of single
 107 lithospheric thickness, and also confidently show that the slab is multiply thickened from
 108 the transition zone downward Sigloch et al. (2008).

109 Thickened slabs in the lower mantle have been attributed to slab buckling and folding
110 through the mantle transition zone Guillou-Frottier et al. (1995); Ribe et al. (2007);
111 Běhounková & Čížková (2008); Lee & King (2011); Cerpa et al. (2014); Billen & Arredondo
112 (2018), with possible slab detachment Čížková et al. (2012). Slab folds have not yet been
113 resolved by tomography, so the exact widening mechanism remains speculative from the
114 observational side.

115 In order to produce slab folding and realistic lower-mantle slab morphologies, numer-
116 ical subduction models often require a fixed overriding plate, i.e. zero trench velocity v_t .
117 Even then, the models predict sub-vertical slab folding only for rather extreme values
118 of model parameters, e. g. a very young subducting plate Garel et al. (2014); Strak &
119 Schellart (2021), and/or if special model setups are considered such as those involving two
120 nearby subduction zones Čížková & Bina (2015); Lyu et al. (2019). Thus the observations
121 of pervasively thickened lower-mantle slabs are generally not predicted in current models
122 of subduction dynamics. The models may lack a first-order mechanism that generates
123 thick lower-mantle slabs.

124 To summarize, there are at least two discrepancies between existing models of sub-
125 duction dynamics and first-order observations. First, current models generally produce
126 trench retreat velocities v_t in excess of those observed at present-day subduction zones,
127 alongside SP velocities v_{sp} and subduction rates v_s that are too slow after first slab-660
128 interaction. Second, models seldom reproduce the tomographically observed, multiply
129 thickened geometries that prevail in the transition zone and lower mantle.

130 This study considers how a weak asthenospheric layer (WAL) beneath the plate can
131 resolve these discrepancies. The presence of a WAL on Earth has been proposed to explain
132 a large range of geophysical observations, including postglacial rebound and gravity data
133 (e.g. Paulson & Richards, 2009), shear-wave tomography Kawakatsu et al. (2009); Barruol
134 et al. (2019), seismic attenuation Debayle et al. (2020), seismic anisotropy Debayle &
135 Ricard (2013); Becker (2017) and electrical conductivity tomography Naif et al. (2013).
136 The viscosity reduction could originate from a plume-fed asthenosphere Phipps Morgan
137 et al. (1995), from the depth-dependency of dislocation creep flow laws Raterron et al.
138 (2011), from crystal-preferred orientation Meyers & Kohlstedt (2021), or from the presence
139 of melt pockets Cooper & Kohlstedt (1986); Chantel et al. (2016), which may remain
140 trapped due to low melt fractions Holtzman (2016) or low density contrast Sakamaki
141 et al. (2013).

142 The presence of a WAL is predicted to affect large-scale dynamics of the underlying,
143 convecting mantle Lenardic et al. (2006), and to favor ‘plate-like’ rather than ‘stagnant-lid’
144 regimes Höink et al. (2012). Since the sub-lithospheric mantle resists a plate’s trenchward
145 motion, the inclusion of a WAL in models of subduction dynamics yields faster subduction
146 velocities v_{sp} , as shown by Carluccio et al. (2019) and Suchoy et al. (2021). The latter
147 authors also showed that increased v_{sp} was coeval with reduced trench retreat v_t , although
148 they did not detail the implications for lower mantle slab morphologies. We hypothesize
149 that increasing subduction rates while reducing trench motion results in the accumulation
150 of slab material in a near-vertical column beneath the (quasi stationary) trench, and that
151 the slab must widen (through folding) around the depths where it slows down to lower-
152 mantle sinking rates, given that slab input v_s remains high. Thus, a WAL could resolve
153 both first-order discrepancies regarding plate velocities and slab morphologies.

154 We carry out a systematic numerical analyses of how a WAL impacts the dynamics
155 of thermo-mechanical subduction models featuring an overriding plate. Section 2 pro-
156 vides a first-order quantification of slab widening behavior in modern subduction zones,

157 using plate kinematic data. Section 3 describes the model setup. Section 4 presents our
 158 modeling results, and Section 5 discusses their implications for subduction systems on
 159 Earth.

160 2 Quantifying slab folding from plate motions and slab 161 sinking rates

162 2.1 Conceptual assessment

163 We start by demonstrating how slab folding can be assessed theoretically as a geomet-
 164 rical/kinematic phenomenon, involving slab accumulation in the mantle transition zone.
 165 This analysis is inspired by subduction models where (unlike our own model) velocities
 166 are applied to one or both plates, and which can predict slab morphology as a function
 167 of these imposed surface kinematics Christensen (1996); Heuret et al. (2007); Arcay et al.
 168 (2008); Gibert et al. (2012); Cerpa et al. (2015); Guillaume et al. (2018); Cerpa et al.
 169 (2018). Among these, Gibert et al. (2012), anchored the subducting slab to a rigid 660-
 170 km discontinuity, which aims to simulate the effect of a strong viscosity jump at 660 km,
 171 as inferred from e.g. geodetic constraints Mitrovica & Forte (2004). Gibert et al. (2012)
 172 showed that if the subduction rate $v_s = v_{sp} + v_t$ exceeds the trench velocity v_t , continued
 173 subduction results in slab folding at the base of the upper mantle. Essentially, the slab
 174 has to fold because trench retreat does not create enough lateral accommodation space
 175 to permit all incoming slab to lie down flat on the '660'. Here we extend their analysis to
 176 the more general case where the subducting slab sinks into the lower mantle.

177 Let $v_s \times \Delta t$ be the length of subducted material consumed at the trench over some
 178 duration Δt . The lateral displacement of the trench over the same duration is $v_t \times \Delta t$. The
 179 displacement of the deepest portions of the subducting slab (simplified as the displacement
 180 of the slab tip) within the upper mantle is approximated as $v_{\text{tip}} \times \Delta t$, where v_{tip} is the
 181 absolute velocity of the deepest point of the slab. Slab folding can thus be understood
 182 as a simple geometrical constraint. When the length of subducted material is larger than
 183 the lateral displacement of the trench plus the displacement of the slab tip, the excess
 184 length (slab accumulation) is expected to be accommodated by folding. Put in another
 185 form, slab accumulation and folding occurs when:

consumption rate of subducted material $>$ trench displacement + slab tip motion in the mantle

186 Alternatively, we can define a kinematic ratio K_r which predicts whether the subduct-
 187 ing slab undergoes folding as:

$$K_r = \frac{v_s}{|v_t| + \sqrt{(v_{\text{tip}}^x)^2 + (v_{\text{tip}}^z)^2}} \quad (1)$$

188 where we have decomposed the velocity of the deepest point of the slab into its horizontal
 189 and vertical components.

190 When $K_r \simeq 1$, the free space created by trench retreat and slab sinking can accom-
 191 modate all newly incoming lithosphere, which does not have to compress (fold). Hence
 192 the slab's apparent thickness remains similar in the upper and lower mantle (Fig. 2).
 193 A kinematic ratio K_r higher than 1 implies a surplus of slab material that cannot be
 194 accommodated by trench retreat and slab sinking into the lower mantle, and instead has

195 to be accommodated by slab folding. At $K_r > 1$, the higher the value of K_r , the greater
 196 the frequency of slab folds (or alternatively, the wider the amplitude of the folds). Also
 197 at $K_r > 1$, the apparent thickness of the folded slab in the lower mantle is predicted to
 198 be multiples of the lithospheric thickness observed in the uppermost mantle.

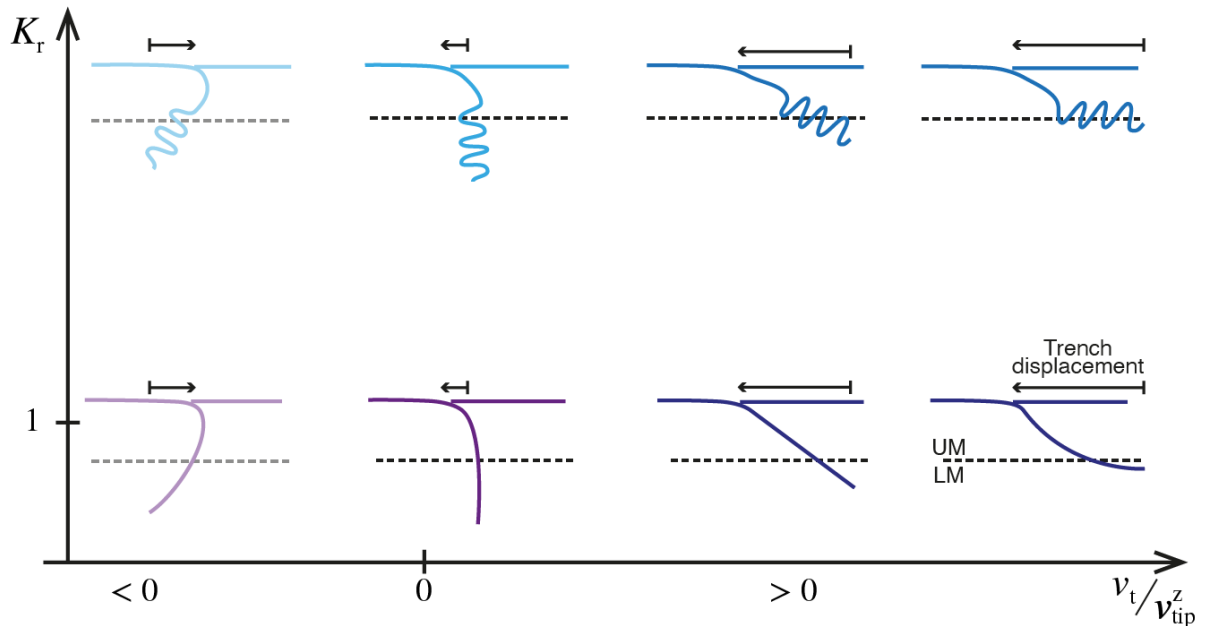


Figure 2: Schematic theoretical diagram depicting various subduction regimes of subducting slabs, well after they have penetrated in to the lower mantle (LM). UM: upper mantle. Dashed line marks the viscosity interface between UM and LM, which we speculatively equate with the seismic ‘660 km’ discontinuity.

199 The ratio of trench velocity to slab-sinking velocity (v_t/v_{tip}^z) controls, to first order, the
 200 average slab dip. This is true for both the unfolded ($K_r \leq 1$) and folded ($K_r > 1$) cases.
 201 Note that we use only the vertical component of the slab-tip velocity as it is thought to
 202 be much higher than the horizontal component (see also below section 2.2).

203 Hence the parameter space along the dimensions of K_r and v_t/v_{tip}^z spans a variety of
 204 candidate slab morphologies and subduction regimes, as depicted in (Fig. 2). For negative
 205 trench motion (trench advance), the subducting slab leans forward, so that the deepest
 206 slab portions lie beneath the subducting plate at increasing distances from the trench
 207 (leftmost regimes in Fig. 2). For quasi-null trench motions, the subducting slab sinks
 208 vertically, with all slab portions remaining below the trench. For relatively high, positive
 209 trench motions (trench “retreat”), the subducting slab leans backwards (“slab rollback”),
 210 with deeper slab beneath the overriding plate. It has been proposed that high trench-
 211 retreat rates promote the complete stagnation of slab atop the 660-km discontinuity Torii
 212 & Yoshioka (2007); Goes et al. (2017), so that high values of v_t/v_{tip}^z may lead to the end-
 213 member subduction regime where the slab flattens and folds on the 660-km discontinuity
 214 (rightmost regimes in Fig. 2).

215 2.2 Estimating slab folding at present-day

216 In order to gauge the prevalence of slab folding in nature, we seek to calculate an ob-
 217 servational estimate of K_r in active subduction zones, using Equation 1. Hence we need
 218 estimates of subduction rate v_s , absolute trench velocity v_t , and slab sinking velocity v_{tip} .

219 For estimating v_s and v_t , we use an updated version of the SUBMAP database Lalle-
220 mand et al. (2005), which defines 249 transects of active subduction zones. Subduction
221 rates are retrieved from the relative plate motions of the MORVEL56-NNR model (based
222 on a circuit of 56 tectonic plates Argus et al. (2011) as explained in the Supporting In-
223 formation Text S1). Each SUBMAP subduction transect is assigned to a subducting
224 plate and an overriding plate of the MORVEL56-NNR plate circuit. For transects that
225 cross significant arc and back-arc deformation, MORVEL56-NNR permits the definition
226 of an “arc block” and assessment of trench motion relative to that of a rigid overriding
227 plate, enhancing the accuracy of the derived subduction rate. For a few subduction
228 zones, the MORVEL56-plate circuit does not account for active arc and back-arc de-
229 formation even though such a deformation has been well-established in the literature
230 (Southernmost-Central Andes, Izu-Bonin, Calabria). For these transects, we complement
231 MORVEL56-NNR with published regional studies (see Supporting Information).

232 To define the absolute motion of the plates and trenches, we need to consider an
233 absolute plate motion model within an absolute reference frame, comparable to the fixed
234 reference frame of our numerical models. In this paper we calculate and compare the value
235 of K_r in three recent absolute plate motion models, constructed in different manners:
236 the “SA” (“spreading-alignment”) model Becker et al. (2015), the “TM25” model Wang
237 et al. (2018), and the “GMHRF-1Ma” model by Doubrovine et al. (2012). The SA model
238 minimizes the angular misfit between spreading-ridge orientations and plate velocities.
239 This plate motion was found to give a good fit to azimuthal seismic anisotropy, a proxy
240 for the shear induced by the relative motion between the tectonic plates and the upper
241 mantle. The TM25 model is based on 25 hotspot tracks under the assumption of fixed
242 hotspots relative to the deep mantle. The GMHRF-1Ma model is based on a global fit of
243 hotspot tracks since the Late Cretaceous, accounting for modest relative motions between
244 the hotspots’ mantle plumes, computed by numerical models of whole mantle convection.

245 We extract the trench-normal component of the plates and trench velocities for com-
246 parison with our 2-D models. In what follows, the absolute and relative velocities at each
247 transect are those of their trench-normal components.

248 The observed subduction rates are non-negative with a median value of 5.3 cm/yr and a
249 long tail up to almost 12 cm/yr (Fig. 3a). In all three reference frames (Fig. 3b-d), absolute
250 trench velocity v_t scatters around slightly positive values with a median values of 0.71 to
251 0.79 cm/yr. This tendency towards slow trench retreat may or may not be significantly
252 different from zero motion (stationary trench), given the large formal standard deviations
253 of almost 3 cm/yr but also the non-Gaussian, heavy tails of the histogram. In any case,
254 two thirds of the subduction transects have trench velocities between -1 and 1 cm/yr
255 in the three absolute plate motion frames. Hence typical present-day trench motion is
256 roughly five times smaller than typical subduction velocities.

257 Estimating K_r also requires an observational estimate of slab sinking rates in the lower
258 mantle. Since slabs are not directly dateable, they have been correlated to the geology
259 of accretionary orogens, which hold the surface record of subduction. The subduction of
260 lithosphere is accompanied by the formation of a volcanic arc at the surface, which often
261 survives and is dateable. Such slab-arc correlations have inferred time-averaged sinking
262 rates of 1.0-1.5 cm/yr for slabs that have penetrated the lower mantle Van Der Meer et al.
263 (2010); Sigloch & Mihalynuk (2013); Domeier et al. (2016); Van der Meer et al. (2018);
264 Mohammadzaheri et al. (2021).

265 Using 1 cm/yr as the slab sinking velocity estimate, 70–80% of subduction transects
266 exhibit values of $K_r > 1$ in all three absolute reference frames (Fig. 4 and Fig. S1). Only

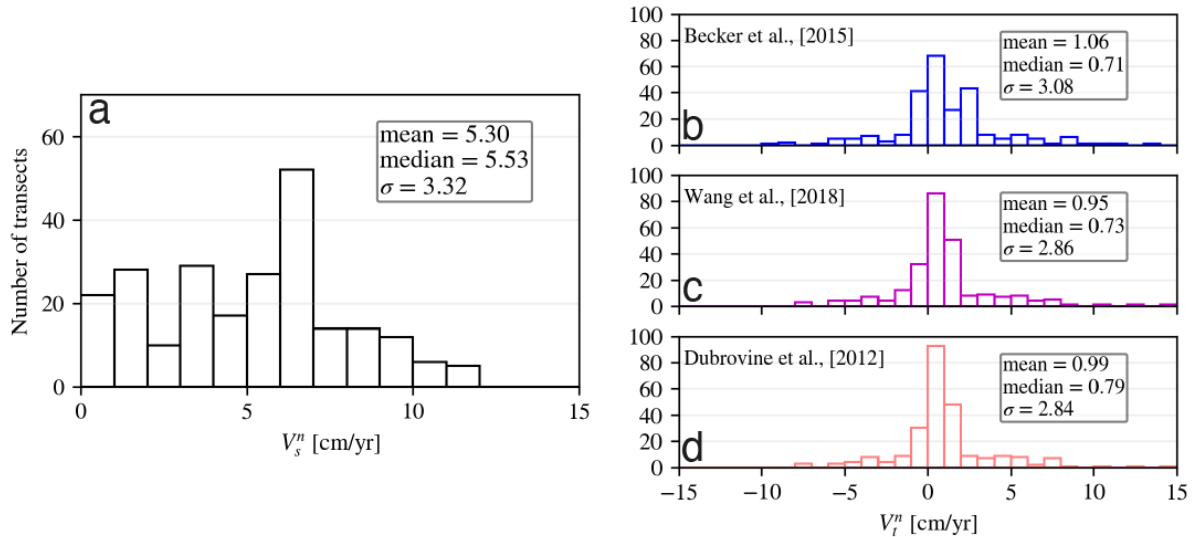


Figure 3: a) Histogram of the trench-normal component of subduction rate v_s in present-day subduction zones. b) Histogram of the trench-normal component of trench velocity (retreat) v_t , in the spreading-alignment reference frame Becker et al. (2015). c) Histogram as in b) but for T25M reference frame Wang et al. (2018). d) Like b), but for GMHRF-1Ma frame Dubrovine et al. (2012).

267 a few subduction transects consistently display $K_r < 1$ in all reference frames, mostly at
 268 the edges of longer arcs: the southernmost Andes (Patagonian transects), the northern
 269 edge of the Lesser Antilles (e.g. Puerto Rico Trench), or the edges of the South Sandwich
 270 SZ.

271 The present-day prevalence of $K_r > 1$ is relatively insensitive to the assumed slab
 272 sinking velocity. Even when considering $v_{tip} = 1.5$ cm/yr, at the high end of the rea-
 273 sonable estimate range ?see e.g. >[]butterworth2014geological,domeier2016global), 63% of
 274 transects remain above $K_r > 1$ in the spreading-aligned absolute plate motion model, and
 275 72% of transects in the two other reference frames.

276 Figure 4a plots the global inventory of slabs (between 600-1800 km depth), from which
 277 the sinking rates were derived. Importantly, most areas are slab free. Existing slabs
 278 cluster in two vast, linear belts: one under the Alpine-Eurasian-Himalayan-southwest
 279 Pacific orogens; the second under the Americas and into Siberia. From the geologic record
 280 and quantitative plate reconstructions, these are the known, absolute locations of major
 281 orogenies over the past 200 million years, hence the known paleo-trench locations. The
 282 observation that slabs are still located only beneath these independently inferred paleo-
 283 trench regions means that slabs sank rather vertically. The vast slab-free mantle areas are
 284 known not to have hosted trenches over the past 200 m.y. This implies that paleo-trenches
 285 have remained quite stationary over a time period during which the areal equivalent of
 286 all ocean basins was subducted once or twice over Coltice et al. (2012). Thus trenches
 287 had the opportunity to migrate across the globe but did not, which indicates sustained
 288 $K > 1$ (slab folding regime) over geologic time.

289 Finally, slab dimensions directly point towards folding. In figure 4a, the Eurasian
 290 and American slab belts are 15,000-20,000 km long; individual slab segments are 1,000-
 291 3,000 km long (i.e., arc length) and 400-700 km wide. The latter is a multiple of litho-
 292 spheric thickness, and suggests slab folds of this amplitude.

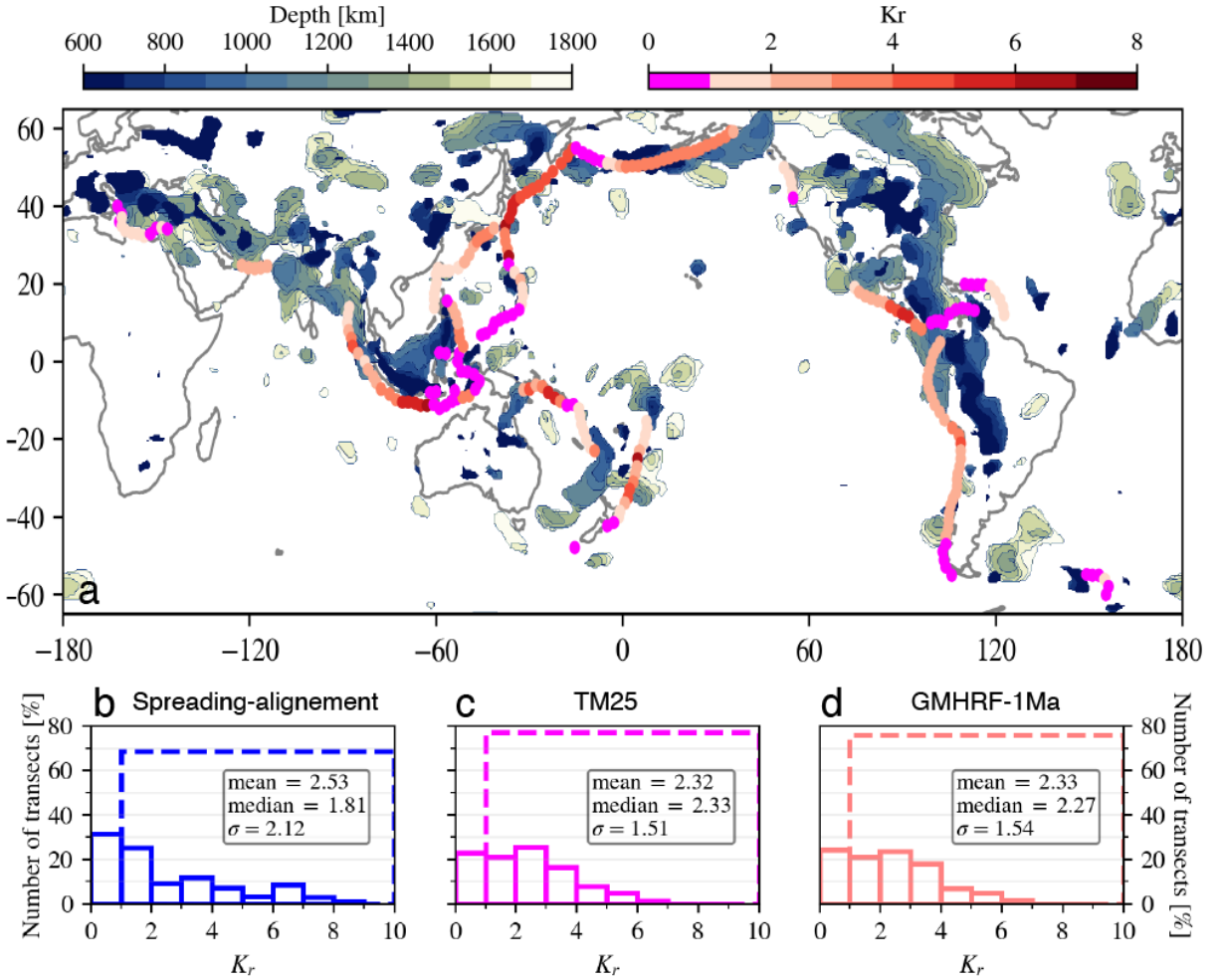


Figure 4: a) Map shows estimates of the kinematic ratio K_r (reddish color scale) for all subduction transects of the SUBMAP database Heuret & Lallemand (2005). The regime of inferred slab folding ($K_r > 1$) prevails in most subduction zones. The absolute plate motion model is GMHRF-1Ma, which yields intermediate K_r values compared to the also-investigated spreading-alignment and TM25 models (plotted in the supplementary information). Also shown in blue shades is the global inventory of subducted slabs in the lower mantle (600-1800 km depth). More precisely, these are contours of seismically fast P-velocity anomalies exceeding $dvp/vp > 0.35\%$ in global model DETOX-P2 Hosseini et al. (2020). b) Histogram of K_r values in the spreading-alignment reference frame. c) Histogram of K_r values in the TM25 reference frame. d) Histogram of K_r values in the GMHRF-1Ma reference frame.

293 Thus three separate lines of observational reasoning suggest that most present and
 294 past subduction zones feature(d) a surplus of subducted material not accommodated by
 295 lateral trench migration and slab sinking, so that instead slab folding is required. As
 296 discussed, common models of subduction dynamics (hereafter referred to as standard
 297 models) seldom reproduce this regime. Next we investigate whether adding a WAL to
 298 a standard model can shift its regimes from non-folding to folding over a wide range of
 299 model parameters.

300 3 Modeling approach

301 We use 2-D thermo-mechanical models of subduction dynamics. The governing equations
 302 are those suitable for multi-material, incompressible viscous flow, under the Boussinesq
 303 approximation, which are solved using the finite-element, control-volume, unstructured
 304 adaptive mesh Fluidity computational modelling framework, which has been carefully
 305 validated for simulations of this nature Davies et al. (2011); Kramer et al. (2012); Le Voci
 306 et al. (2014); Kramer et al. (2021). Our model setup and material properties are similar
 307 to Garel et al. (2014), albeit that in some cases we extend the models by incorporating a
 308 sub-lithospheric weak asthenospheric layer (WAL), similar to that in Suchoy et al. (2021).
 309 Below we summarize our modeling approach.

310 3.1 Model Setup

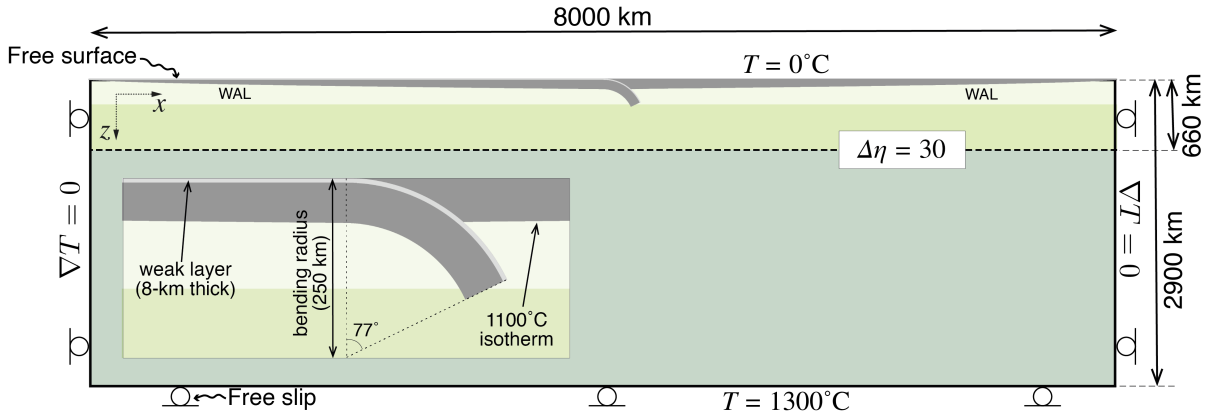


Figure 5: Model setup and boundary conditions. In the standard models the viscosity of the WAL is equal to that of ambient mantle ($\alpha = 1$), i.e., no weak asthenospheric layer (WAL) is present. We implement a viscosity contrast $\Delta\eta$ of 30 at 660-km depth, the boundary between upper and lower mantle. The initial curved geometry of the subducting plate is prescribed using a bending radius of 250 km, including the weak layer.

311 The model predicts the evolution of an isolated subduction zone comprising both a
 312 subducting plate (SP) and an overriding plate (OP), with no external forces or velocities
 313 applied to the system. The model domain is a Cartesian box that is 8000-km wide and
 314 2900-km in height (i.e. the whole mantle depth). Mechanical boundary conditions on the
 315 sides and base of the domain are free-slip, with a free-surface at the top. We use no-flux
 316 thermal boundary conditions on the sides and impose constant temperatures of 0°C and
 317 1300°C at the surface and at the bottom boundaries, respectively.

318 The initial temperature field is given by a half-space cooling model where the age of
 319 the plates vary linearly from the 0 at the ridges to (A_{SP}) for the subducting plate and to
 320 (A_{OP}) for the overriding plate. Models begin with a curved subducting slab to initiate
 321 subduction (see inset Fig. 5). Below the plates, the initial mantle temperature is equal to
 322 that of the bottom boundary.

323 We consider a composite visco-plastic rheology that accounts for four deformation
 324 mechanisms: linear diffusion creep, and non-linear dislocation creep, Peierls creep and

325 pseudo-brittle yielding. The effective viscosity is:

$$\frac{1}{\eta_{eff}} = \left(\frac{1}{\eta_{diff}} + \frac{1}{\eta_{disl}} + \frac{1}{\eta_P} + \frac{1}{\eta_Y} \right) \quad (2)$$

326 which is bounded at lower and upper limits.

327 The diffusion (η_{diff}), dislocation (η_{disl}) and Peierls (η_P) viscosities follow the generic
328 form:

$$\eta_{diff|disl|P} = A^{\frac{1}{n}} \exp\left(\frac{E + PV}{nRT_r}\right) \dot{\epsilon}_{II}^{\frac{1-n}{n}} \quad (3)$$

329 where A is a prefactor, n is the stress exponent, E and V are the activation energy and
330 volume, respectively. P is the lithostatic pressure, R the gas constant, and $\dot{\epsilon}_{II}$ the second
331 invariant of the strain-rate tensor. T_r is the sum of model temperature and an adiabatic
332 temperature gradient of 0.5 °C/km and of 0.3 °C/km in the upper and lower mantle,
333 respectively. The pseudo-brittle yielding viscosity follows a yield-stress law

$$\eta_Y = \frac{\tau_Y}{2\dot{\epsilon}_{II}} \quad (4)$$

334 where the yield strength $\tau_Y = \min(\tau_0 + f_c P, \tau_Y^{\max})$, with τ_0 the surface yield strength, f_c
335 the friction coefficient, P the lithostatic pressure, and τ_Y^{\max} the maximum yield strength.
336 The weak layer is 8-km thick, with a friction coefficient 10 times lower than the mantle
337 material, and a maximum prescribed viscosity of 10^{20} Pa s. All rheological parameters
338 are as in Table 1 of Garel et al. (2014) and we use a consistent solution strategy.

339 3.2 Treatment of WAL

340 The depth extent of a potential WAL is not well constrained. Some studies, which consider
341 it to be a layer of partial melt, suggest that it is only 10-20 km thick Schmerr (2012);
342 Sakamaki et al. (2013); Stern et al. (2015), whereas others advocate for a layer extending
343 from the lithosphere-asthenosphere boundary up to 200-300 km depth (thus a thickness of
344 approximately 100-200 km) Kawakatsu et al. (2009); Paulson & Richards (2009); French
345 et al. (2013); Becker (2017); Barruol et al. (2019); Debayle et al. (2020). Here, we simulate
346 the presence of the WAL by imposing a viscosity reduction between the 1100 °C isotherm
347 (a proxy for the LAB) and a depth of 220 km, similarly to Suchoy et al. (2021). Note
348 that models tested with a WAL extending up to 300 km depth showed little differences
349 with the results reported below. We define the effective viscosity within the WAL as:

$$\eta_{WAL} = \alpha \eta_{eff} \quad (5)$$

350 where $0 < \alpha \leq 1.0$ is a reduction-viscosity factor.

351 The viscosity reduction of a WAL, and its origin, is also debated. For example, partial
352 melt can lead to a 20-fold or larger viscosity reduction Holtzman (2016), but strongly
353 depends on melt fraction, creep regime, grain size and wetting angle Kohlstedt & Zim-
354 merman (1996). Milder viscosity reduction (< 5-fold) are expected from crystal-preferred
355 orientation considerations Meyers & Kohlstedt (2021). We choose here to explore values
356 of α in [0.2; 0.5; 1.0] (respectively, a viscosity reduction of 5-, 2-, or zero-fold – see below
357 Section 4.1). Note that larger viscosity reductions (α of 0.01-0.1) have usually been used
358 in global mantle flow models reproducing sub-plate seismic anisotropy Conrad & Behn
359 (2010); Becker (2017). However, values of α lower than 0.1 in our set-up led to unre-
360 alistically large asthenospheric flow velocities (>50 cm/yr) and to thermal instabilities
361 potentially associated to small-scale convection (further discussion in Section 5.3.1).

362 4 Model results

363 We first perform a set of simulations without a WAL ($\alpha = 1$), that we hereafter refer to as
 364 standard cases. Next, we explore sets of simulations with different degrees of weakening
 365 in the WAL (i.e. various values of α), that we refer to as WAL cases. For each case,
 366 we define a reference simulation (with plate ages $A_{sp} = 40$ My and $A_{op} = 20$ My). We
 367 subsequently run simulations that span a range of initial ages to cover a wide range of
 368 strength and buoyancy for both plates, while being representative of all regions of the
 369 subduction regime diagram presented in Garel et al. (2014).

370 4.1 Standard cases - no WAL

371 4.1.1 Reference simulation [$A_{sp} = 40$ My; $A_{op} = 20$ My]

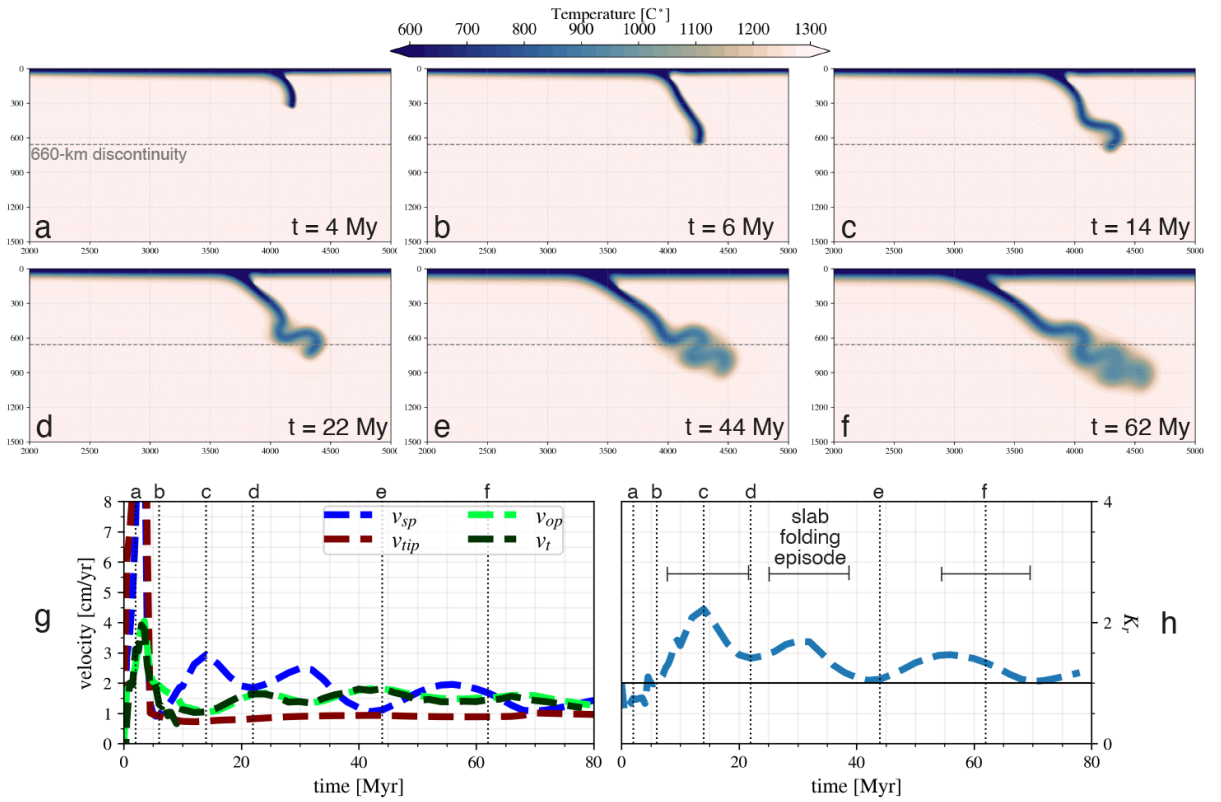


Figure 6: Reference standard model, featuring $A_{sp} = 40$ and $A_{op} = 20$ My. (a-f) Temporal snapshots of the evolution of the temperature field, from 4 to 62 My. g) Kinematics of plates, slab, and trench. v_{sp} in dark blue, positive to the right. v_{op} in green, positive to the left. v_t in light blue, positive to the left. v_{tip} in dark red is the magnitude of slab tip velocity in. Vertical dashed lines mark snapshots times of (a-f). h) Temporal evolution of Kinematic ratio K_r , a proxy for the slab’s propensity to fold (definition in the text). Horizontal black line denotes the boundary between the folding ($K_r > 1$) versus non-folding ($K_r < 1$) regime.

372 Figure 6 displays the temporal evolution of the reference simulation for the standard
 373 cases ($\alpha = 1$). During the first stage of free-sinking through the upper mantle (Fig. 6a), the
 374 subducting plate accelerates as slab pull increases with increasing slab length, reaching

375 a peak velocity of ~ 13 cm/yr with trench retreat/OP velocity peaking at ~ 4 cm/yr
 376 (Fig. 6g). Since trench velocity is very similar to OP velocity, indicating little back-arc
 377 deformation, we will only describe the evolution in terms of trench velocity. As soon as
 378 the slab tip encounters the high-viscosity lower mantle at $t \simeq 5$ My, the plate velocities
 379 decrease to between 1 and 3 cm/yr. This slab-660 interaction is followed by two subsequent
 380 episodes of slab folding. First, the slab bends with an OP-wards concavity between ~ 6
 381 and ~ 14 My (Fig. 6b-c), with an increase in SP velocity (up to 3 cm/yr) and low trench
 382 velocity of approximately 1 cm/yr. Then, a transient stage of slab rollback, associated
 383 with a slight increase in the trench velocities up to 1.5 cm/yr, lasts for approximately
 384 5 My (Fig. 6c) and lowers slab dip in the upper mantle. The second folding episode
 385 occurs between ~ 25 and ~ 40 My: the deeper, folded portion of the slab flattens above
 386 the lower mantle while the shallow slab continues to roll back (Fig. 6d), increasing slab
 387 pull (v_{sp} up to ~ 2.5 cm/yr). Another transient stage of trench retreat without buckling
 388 follows (Fig. 6e), with trench velocity (1.8 cm/yr) greater than the SP velocity (1 cm/yr).
 389 From 50 My, a third slab-folding episode occurs, but with a smaller amplitude due to the
 390 obliquity of slab relative to the viscosity jump (Fig. 6f), and a smaller increase in v_{sp} .
 391 Overall, through time, all velocities decrease and tend towards 1 cm/yr, comparable to
 392 the sinking velocity of the deepest part of the slab within the lower mantle. Slab sinking
 393 rates in the lower mantle therefore strongly modulate, and perhaps even limit, surface
 394 kinematics.

395 The kinematic ratio, K_r , given in Equation 1 provides an alternative quantitative
 396 diagnostic. During the free-sinking stage, the slab-tip velocity reaches a peak value of
 397 20 cm/yr, higher than the peak SP velocity v_{sp} (13 cm/yr). As a consequence, the kine-
 398 matic ratio $K_r \leq 1$ (Fig. 6g). After the slab has interacted with the 660-km discontinuity
 399 K_r display oscillations. These oscillation follow those observed for v_{sp} and v_t , when one
 400 of the two increases while the other decreases. Folding episodes occur when $K_r > 1$,
 401 while slab-retreating stages occurs for lower $K_r \simeq 1$. Through time, the amplitude of K_r
 402 oscillations decrease, reflecting the decrease in folding as the slab inclines and the impact
 403 angle with the 660-km viscosity discontinuity decreases.

404 4.1.2 Slab morphologies and kinematic ratios across all standard cases

405 We run a series of no-WAL simulations with various initial plate ages (20-100 for the
 406 overriding plate; 10-100 for the subducting plate). Since we focus on the long-term evolu-
 407 tion of these systems (i.e. well after the first stage of slab-free sinking through the upper
 408 mantle), Figure 7a only displays their state at $t = 80$ My.

409 Several studies have focused on the interaction and passage of slabs through the mantle
 410 transition and the resulting slab morphologies Torii & Yoshioka (2007); Billen (2010); Lee
 411 & King (2011); Čížková & Bina (2013); Billen & Arredondo (2018), sometimes character-
 412 izing a range of so-called subduction regimes Garel et al. (2014); Agrusta et al. (2017);
 413 Li et al. (2019); Briaud et al. (2020). Here we focus on two features after initial slab-660
 414 interaction: trench motion and the amount of slab folding. Thus we define three regimes:
 415 strong trench retreat without slab folding (SR), strong trench retreat with slab folding
 416 (SRwF), and a weak trench retreat with slab folding (WRwF) (7a). The strong-retreat
 417 modes are those for which the total displacement of the trench during the simulation
 418 amounts to an average rate higher than 1 cm/yr, and weak-retreat modes when it is
 419 ≤ 1 cm/yr. Following, Garel et al. (2014), the results of simulations are reported as func-
 420 tions of initial SP and OP ages, with the former controlling slab buoyancy and resistance
 421 to bending, and the latter controlling the OP bending resistance opposing trench retreat.

422 Note that due to our focus on the long-term trench motion and the tendency and nature
423 of slab folding, the subduction regimes outlined herein differ from those used in Garel
424 et al. (2014).

425 The SR regime in the simulations of the standard case occurs for both relatively
426 old SPs and relatively old OPs. The regime WRwF occurs only for very young SPs.
427 The regime that lies in between, SRwF, occurs over the widest parameter space. In
428 simulations with relatively young OPs, only the SRwF is observed. For extremely young
429 cases ($A_{SP} = A_{OP} = 20$ Myr), subduction is rapidly terminated through slab detachment,
430 because the low slab pull cannot initially overcome the resisting forces.

431 Figure 7b displays the evolution of K_r for four selected standard simulations. These
432 simulations display peak K_r of 1.5-2.2, shortly after the first slab-660 interaction (time
433 range 5 to 20 Myr). Simulations [$A_{sp}=40$ My ; $A_{op}=20$ My] (ref. simulation - SRwF) and
434 [$A_{sp}=40$ My ; $A_{op}=65$ My] (SRwF) display oscillations of K_r associated with slab folding.
435 Simulations [$A_{sp}=65$ My ; $A_{op}=65$ My] (SR) and [$A_{sp}=100$ My ; $A_{op}=65$ My] (SR) display
436 $K_r \sim 1$ at all times after initial slab-660 interaction. At later times, the value of K_r tends
437 to 1, associated a decrease of both v_{sp} and v_s (see Figure S6 of Supp. Inf.).

438 4.2 WAL cases

439 We next perform simulations with a WAL, that is simulations where we impose values of
440 the weakening factor $\alpha < 1$ in the sub-lithospheric mantle.

441 4.2.1 Reference WAL simulation with $\alpha = 0.5$ ($A_{sp}=40$ My and $A_{op}=20$ My)

442 In the reference WAL simulation (Fig. 8), the first slab-660 interaction occurs at ~ 1.5
443 My, earlier than in the comparable standard simulation ($\simeq 4$ My). The first slab buckling
444 episode occurs shortly after at 2-10 My (Fig. 8a-b), with subducting plate and trench
445 velocities of 5.5 cm/yr and 1 cm/yr, respectively. A second folding episode takes place
446 after 10 My (Fig. 8c-d) during which the SP velocity increases from 1.8 to 3.8 cm/yr
447 between $t = 14$ My and $t = 22$ My and that of the trench decreases from 1.8 to 0.8 cm/yr.
448 The next folding episode (between $t = 35$ My and $t = 55$ My, Fig. 8e) is associated with
449 a stationary trench, while the SP velocity stabilizes at ~ 2.5 cm/yr. A third fold forms
450 after $t = 55$ My (Fig. 8f) which produces a peak subducting-plate velocity of 4.8 cm/yr.

451 The opposite evolution of trench and SP velocity, associated with K_r oscillation, is
452 even more apparent than in the reference simulation of the standard case. After the first
453 slab-660 interaction, the slab tip velocity remains nearly constant at around 1 cm/yr,
454 independent of slab folding and oscillation of surface velocities.

455 4.2.2 Mantle drag forces on the subducting plate

456 Differences in the evolution of reference simulations can be explained by a reduction of
457 mantle drag at the base of the subducting plate. We calculate a drag force as the integral
458 of the tangential stress along the 1100°C isotherm (in N m^{-1}). Figure 9 displays the
459 temporal evolution of this diagnostic for the reference simulations (i. e, with and without
460 a WAL).

461 Prior to initial slab-660 interaction, both models show sub-lithospheric mantle moving
462 towards the trench but with velocities reduced relative to overlying lithosphere (Couette-
463 flow type). Shear stresses beneath the subducting plate are positive and mostly negative
464 beneath the overriding plate. Shear stresses along the base of the subducting plate remains

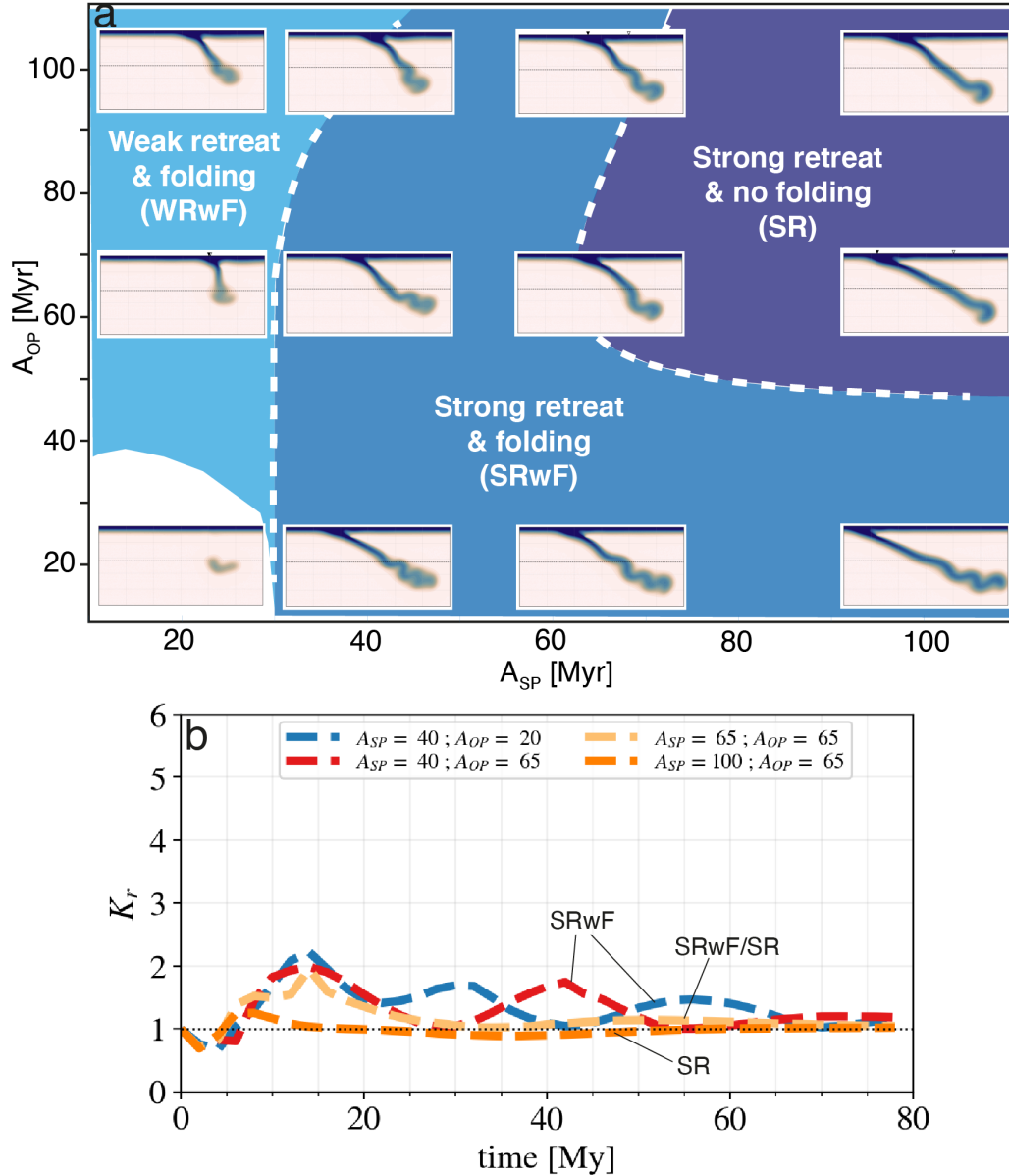


Figure 7: a) Snapshots of the final state (after model run times of 80 My) of all standard models superimposed on a regime diagram. The three regimes are: strong trench retreat without slab folding (SR, purple), strong trench retreat with slab folding (SRwF, dark blue), and weak trench retreat with slab folding (WRwF, light blue). The boundaries between regimes are approximate. b) Kinematic ratio K_r as a function of the time since the initiation of subduction, for four of the standard models shown in (a). The subduction regimes associated with the evolution of those models is indicated by labels. Over time, all four models tend towards no-folding ($K_r \approx 1$).

465 positive after initial slab-660 interaction (Fig. 9c,e), and the drag force remains negative.
 466 Overall, we observe that the absolute value of the drag force beneath the subducting plate
 467 decreases with time as a consequence of the reduction in the length of that plate with
 468 time.

469 The two simulations display similar oscillatory trends that reflect slab folding behavior.
 470 However, as expected, the absolute drag is lower in the simulation featuring a WAL,

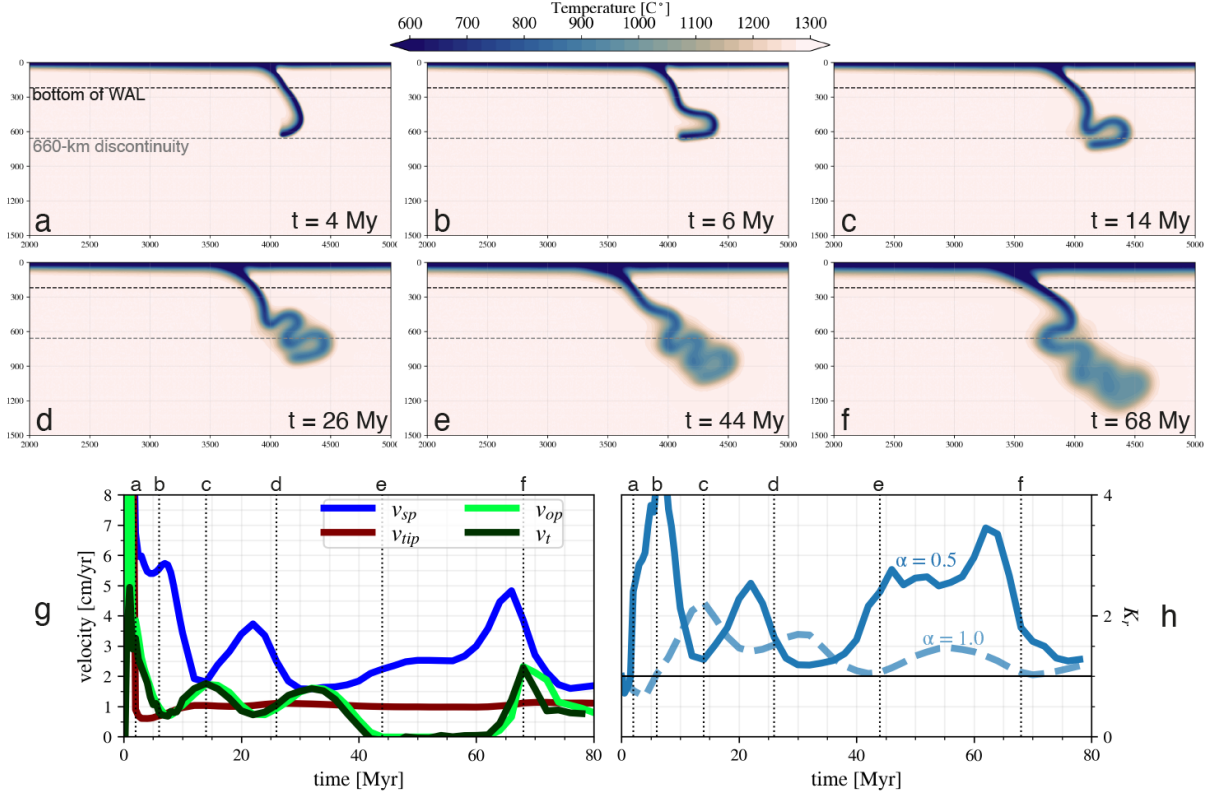


Figure 8: Reference simulation [$A_{sp}=40$ Myr ; $A_{op}=20$ Myr] of the WAL case with a two-fold viscosity reduction ($\alpha = 0.5$). Panels and plotting styles as in Fig. 6. Panel (h) displays the evolution of K_r for this reference WAL case (solid blue) and also for the reference standard case of Fig. 6 (dashed blue).

471 explaining the higher SP velocities observed in this case (Fig. 8g) relative to the compara-
 472 ble no-WAL case (Fig. 6g). The faster subducting plate may hamper trench retreat with
 473 faster trench-wards asthenospheric flow opposing slab rollback Alsaif et al. (2020). Slab
 474 sinking, and hence a faster subducting plate, may also be enhanced through dislocation
 475 creep decreasing the viscosity of adjacent asthenosphere, further facilitating slab descent
 476 Garel et al. (2020). All these effects favor the higher K_r observed in the reference WAL
 477 case compared to the reference standard case.

478 4.2.3 Subducting slab morphologies and kinematic ratios in the WAL case

479 As with the standard cases, we run a series of WAL simulations with $\alpha = 0.5$ spanning
 480 plate ages that range from 20-100 Myr. Figure 10a displays their final state at 80 Myr,
 481 together with the inferred regime diagram. Consistent with the standard cases, WAL
 482 cases exhibit three regimes (SR, SRwF, and WRwF), but regime boundaries are shifted
 483 towards higher plate ages. In particular, the WAL simulations [$A_{sp}=65$ Myr- $A_{op}=65$ Myr]
 484 and [$A_{sp}=65$ Myr- $A_{op}=100$ Myr] now lie more clearly in the SRwF regime while their
 485 standard equivalents belong to the SR regime. Moreover, the WAL simulations with
 486 $A_{sp} = 40$ Myr lie within, or very close to, the WRwF regime, whereas for standard cases,
 487 only those with $A_{sp} \geq 20$ Myr are within this regime.

488 Figure 10b displays the kinematic ratio K_r of selected WAL simulations. As in the
 489 standard cases, the ratios K_r before and during the first slab-660 interaction is generally

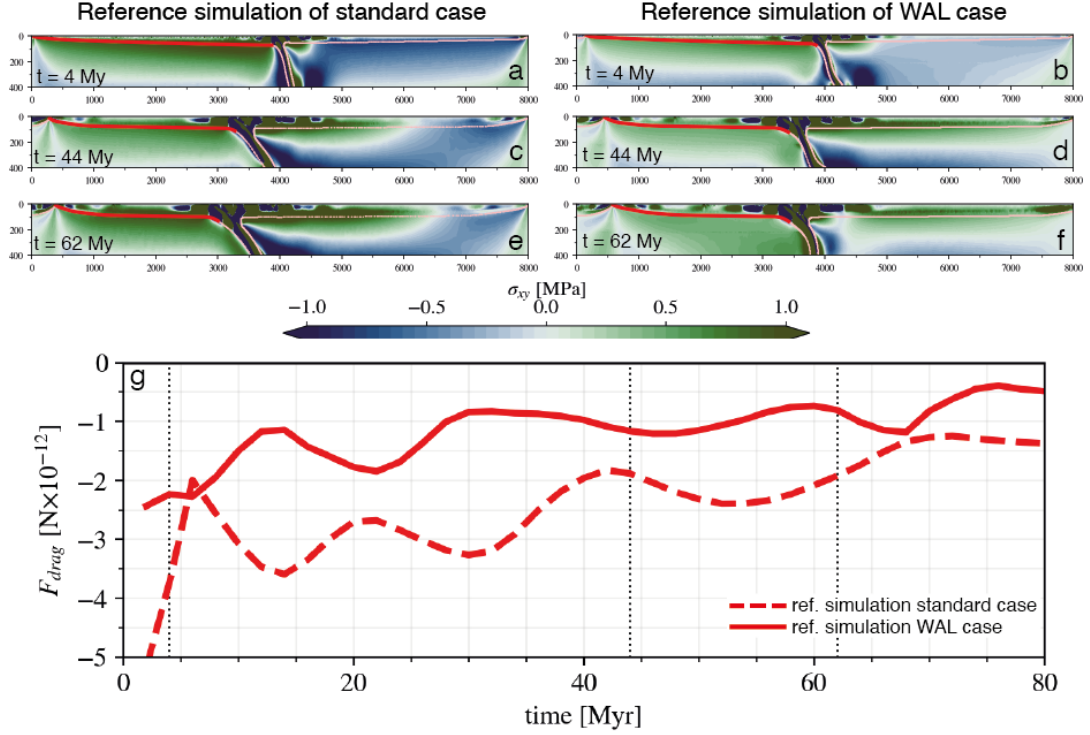


Figure 9: Viscous mantle resistance acting below the subducting plate in the reference standard model versus in the reference WAL model. (a,c,e) Snapshots of the shear stress field (background colour) the reference standard model at times 4 My, 44 My, and 62 My. (b,d,f) Same snapshots for the reference WAL model. Red line traces the LAB isotherm of 1100°C (pink) used to calculate the drag below the subducting plate. Positive shear stresses imply that the tangential component of the stress vector - calculated along the quasi-horizontal LAB isotherm of the subducting plate - is toward the left. g) Evolution of the mantle drag force below the subducting plate for the reference standard model (dashed red) and the reference WAL model (solid red) . Negative values denote a force toward the left. The total mantle drag force onto the subducting plate is negative in accordance with the stress vector. Three vertical dashed lines indicate the times of the snapshots (a-f). The drag force beneath the overriding plate is less straightforward to analyze, see Supporting Information section S4.

490 higher than 1. Some peak values of K_r reached in the WAL simulations are even greater ($>$
491 2) than the highest values observed in the standard simulations (7b). Most importantly,
492 two of these simulations [$A_{sp} = 40$ My; $A_{op} = 20$ My] (ref. simulation for the WAL case)
493 and [$A_{sp} = 65$ My; $A_{op} = 65$ My] display $K_r > 2$ even after the first slab-660 interaction:
494 the presence of a weak layer favors the excess accumulation of subducted material in the
495 mantle relative to the accommodation by motion of both the trench and slab tip, resulting
496 in substantial slab folding. The simulation [$A_{sp}=100$ My ; $A_{op}=65$ My] shows values of K_r
497 close to 1 at all times after initial slab-660 interaction, consistent with the standard case,
498 lying in the SR regime. WAL simulation [$A_{sp}=65$ My ; $A_{op}=65$ My] exhibits intermediate
499 behavior, with oscillations of K_r up to 1.5, while its standard equivalent show values close
500 to 1. This is because the former clearly lies in the SRwF regime while its equivalent
501 standard case lies near the transition from the SRwF to the SR regime.

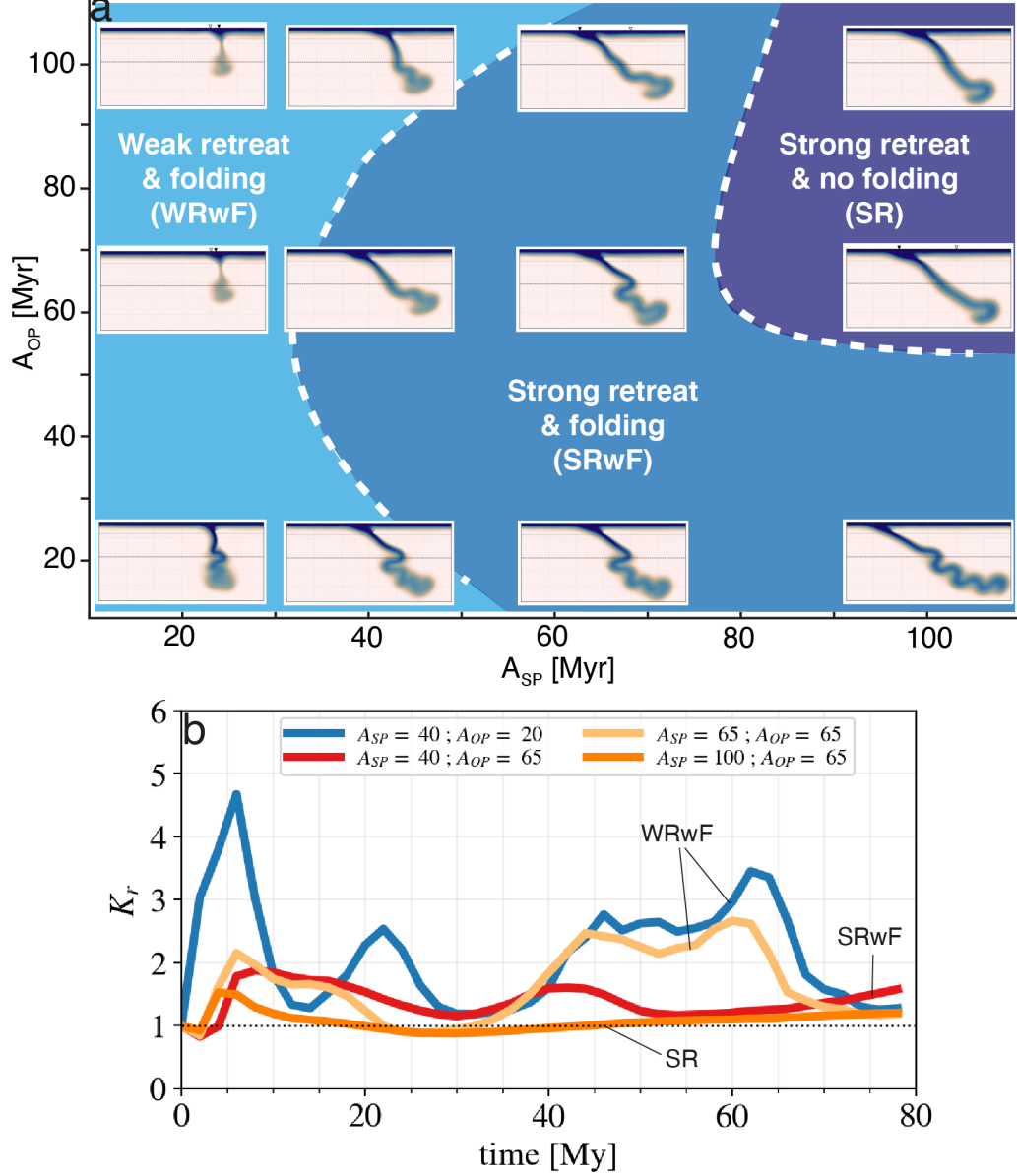


Figure 10: a) Regime diagram of WAL models with two-fold viscosity reduction ($\alpha = 0.5$). Panels and plotting styles as in Fig. 7.

502 4.2.4 WAL cases with $\alpha = 0.2$

503 We finally run a series of simulations for a WAL with $\alpha = 0.2$ (Fig. 11a). The most
 504 striking difference, relative to all previous cases examined, is that the SR regime no longer
 505 appears within the range of plate ages investigated: slab folding behavior is consistently
 506 observed, throughout the investigated parameter space. Moreover, the boundary between
 507 the WRwF and SRwF regimes shifts to values of subducting plate ages higher than 65
 508 My and for overriding plate ages higher than 20 My. Hence, strong retreat ($v_t > 1$ cm/yr)
 509 now only occurs for heavy and stiff plates, with the WRwF regimes becoming dominant.
 510 In particular, when the overriding plate is relatively weak ($A_{op} \simeq 20$ My) vertical slab
 511 folding piles in the lower mantle are ubiquitous. Cases also exhibit higher K_r values
 512 (1.5-4) well after the first slab-600 interaction (Fig. 11b).

513 Finally, it is worth noting that in the majority of the above simulations with a WAL

514 and $\alpha = 0.2$, thermal instabilities form within the weak layer at the base of the plates.
 515 These transient instabilities, which take the form of drips of cold lithosphere generated
 516 beneath both overriding and subducting plates, develop as the lithosphere thickens in
 517 response to conductive cooling. The drips are then advected by lateral mantle flow and
 518 mix with underlying mantle. We note that they only occur when the asthenospheric
 519 viscosity reaches values close to or below $\sim 10^{19}$ Pa s, as advocated by previous studies
 520 van Hunen et al. (2003); Ballmer et al. (2011); Le Voci et al. (2014); Davies et al. (2016).
 521 Further analyses of these features will be the focus of a future study.

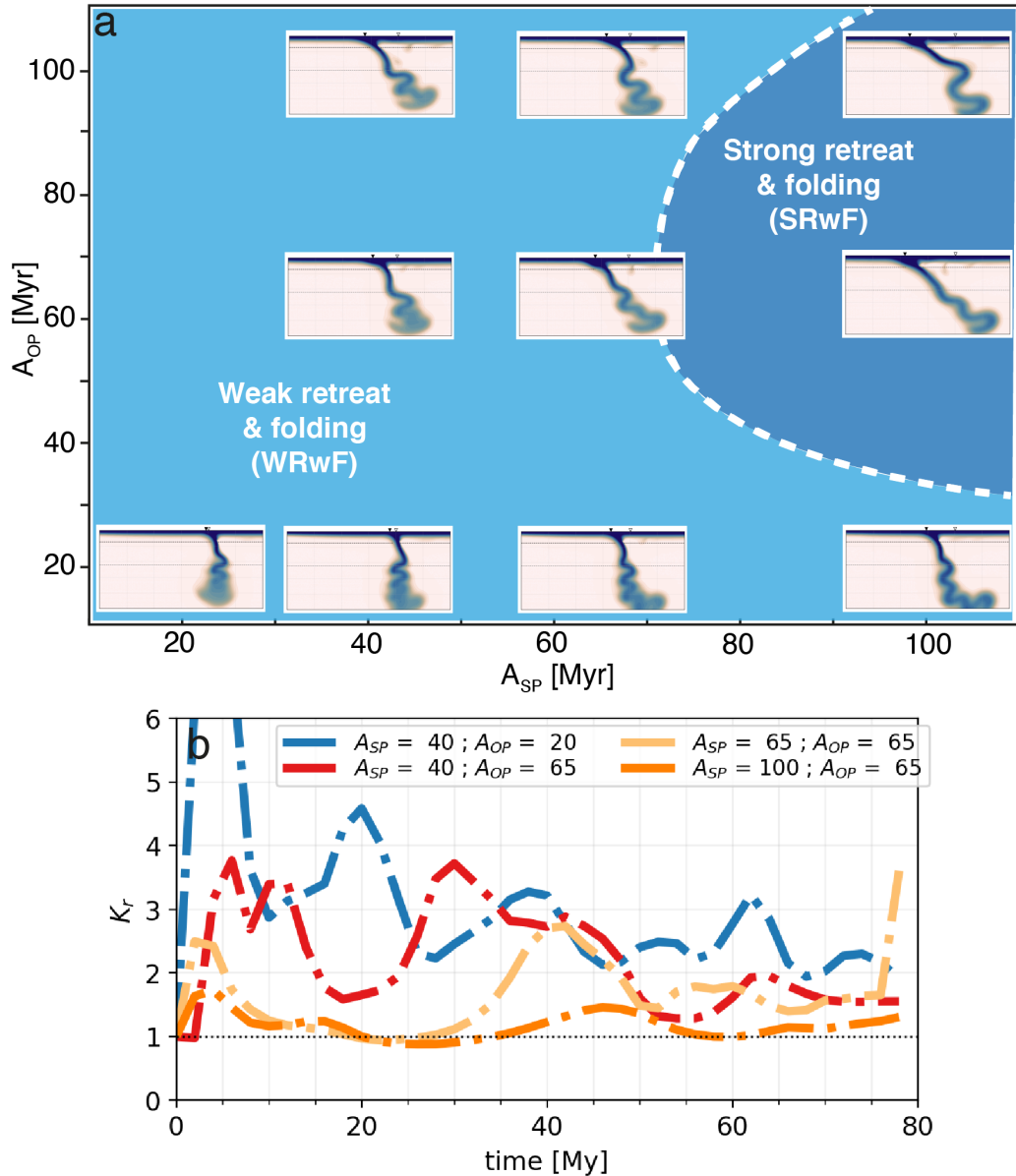


Figure 11: Regime diagram of WAL models with a five-fold viscosity reduction ($\alpha = 0.2$). Panels and plotting styles as in Fig. 7. The models remain in the weak retreat and folding regime over the entire run time, unless they feature very old plate ages.

522 5 Discussion

523 5.1 Surface velocities and kinematic ratios

524 On Earth, subduction rates are typically 3 to 5 times higher than absolute trench veloci-
525 ties, and 5 times higher than estimated slab sinking velocities (see Section 2). This yields
526 kinematic ratio K_r estimates above 1 for most subduction zones, creating a scenario that
527 favours a slab thickening/folding regime (see section 2.2).

528 Simulations without a WAL produce surface kinematics at odds with these obser-
529 vational constraints because once the slab has interacted with the transition zone, the
530 subducting plate v_{sp} slows down to approach slab sinking rates of 1 cm/yr. The addition
531 of a WAL renders the simulations more compatible with observational constraints, in that
532 v_{sp} up to 5 cm/yr are maintained long after initial slab-660 interaction (Fig. S4-S5 in Supp
533 Info), and trench velocities v_t are attenuated to typically lower than 1 cm/yr. Our models
534 with WAL thus reproduce the rapid subduction rate, near-stationary trenches, and slow
535 slab-sinking rates observed on Earth. WAL simulations have higher K_r values than the
536 standard models, as summarized by Figure 12. The time-averaged kinematic ratio \bar{K}_r
537 (after initial slab-660 interaction, i.e., averaged between 20-80 My) ranges from 1.0–1.3
538 in the standard models (Fig. 12a, except for the youngest SP plate ages). In contrast, \bar{K}_r
539 ranges between 1.0–3.1 in WAL simulations with two-fold weakening ($\alpha = 0.5$, Fig. 12b),
540 and between 1.0–2.9 for five-fold weakening ($\alpha = 0.2$, Fig. 12c). \bar{K}_r is generally higher
541 in WAL simulations with $\alpha = 0.2$ (although the maximum value of $\bar{K}_r = 3.1$ occurs for
542 $\alpha = 0.5$ and the youngest plate ages).

543 WAL simulations also show higher peak values of (non-averaged) K_r , before and after
544 first slab 660-interaction. In the standard models, K_r mostly ranges between 1–2 (see
545 Fig. 7 and Supp Info Fig. S6a), whereas the WAL simulations exhibit peak K_r values
546 above 2 and up to 6-7 (Figs. 10 and Fig. 11 – see also Figs. S6b,c in Supp. Info.). Hence
547 only the models with a weak layer produce kinematic ratios K_r that are comparable to
548 those estimated for subduction zones in nature (Fig. 4).

549 Behr & Becker (2018) have suggested the lubrication effect of a weak sedimentary layer
550 above the subducting plate as an alternative mechanism for increasing v_{sp} in models of
551 subduction dynamics ?see also>[[duarte2013three. They showed that v_{sp} could increase by
552 one to two orders of magnitude if sediments reduced viscous resistance at the interface by a
553 comparable amount. However, recent models have shown that a weaker plate interface also
554 favors an increase in trench retreat v_t Pusok et al. (PREPRINT); Behr et al. (2022). We
555 investigated this by running a simulation without a WAL but featuring a plate interface
556 layer with a two-fold reduction in maximum viscosity (see Fig. S8). Relative to our
557 comparable standard case, both v_{sp} and v_t increased slightly, resulting in a negligible
558 difference to K_r . This suggests that a weaker plate interface would not allow us to
559 reconcile model predictions with the available observational constraints on K_r , further
560 supporting an important role for a WAL.

561 5.2 Slab morphologies

562 The presence of a WAL strongly impacts the subduction regimes and lower mantle slab
563 morphologies, as encapsulated by the proxy of K_r . Simulations without a WAL pro-
564 duce low-to-moderate values of K_r , and moderate-to-high trench retreat rates. Without a
565 WAL, strong-retreat regimes are thus dominant across the parameter space examined, and
566 only models with the youngest, weakest overriding plate (20 My) exhibit some slab-folding

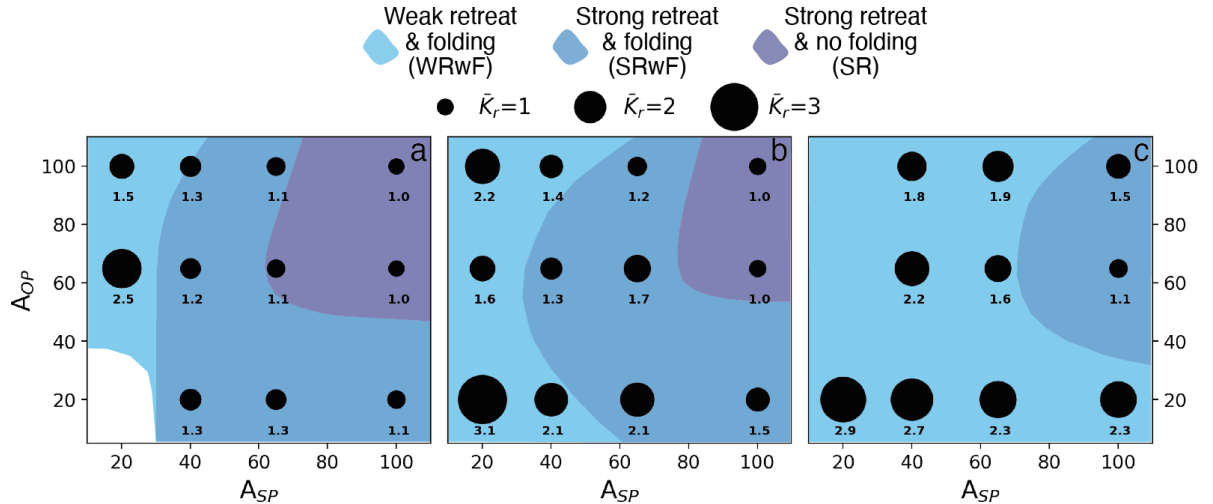


Figure 12: Summary of modeling runs and regime diagrams. Time-averaged kinematic ratio \bar{K}_r after the first slab-600 interaction, plotted in the two-dimensional space of SP and OP plate ages (unit Myr). for (a) standard non-WAL models; (b) WAL models with $\alpha = 0.5$; (c) WAL models with $\alpha = 0.2$. \bar{K}_r is represented by black dots with sizes proportional to \bar{K}_r values, which are also printed. Background colors denote folding regimes as in previous figures. The time-averaging window for obtaining \bar{K}_r is [20-80] My.

567 behaviour. However, even for a WAL with a moderate viscosity decrease ($\alpha = 0.2$), the
 568 (non-folding) SR regime disappears and the SRwF regime only occurs in simulations with
 569 relatively stiff and buoyant plates ($A_{sp} > 80$ My, $A_{sp} > 40$ My). Hence, Slabs folding and
 570 vertically piling in the lower mantle, beneath near-stationary trenches, become the pre-
 571 prevailing morphologies of the WAL simulations (light blue shading in Fig.12). These results
 572 demonstrate, for the first time, that models of subduction dynamics (without external
 573 forcing) are able to produce lower-mantle slab morphologies observed by tomography,
 574 while also honouring the plate and trench velocities measured at the surface.

575 We note that the amplitude of lower-mantle slab folds in our simulations is consistent
 576 with theoretical predictions based on a thin-sheet mathematical formulation. Ribe (2003)
 577 and Ribe et al. (2007) used these formulations to derive a scaling law for the amplitude
 578 of folds of a vertically descending, viscous sheet that buckles as it encounters resistance
 579 at a sharp viscosity jump, or a rigid barrier. The predicted fold amplitude is half the
 580 fall height, which would be half the thickness of the upper mantle in the context of
 581 subduction: approximately 330 km. Our simulations with more pronounced vertical slab
 582 folding produce 300 to 500-km wide folds in the lower mantle, that are consistent with
 583 this theory. We note that the presence of a WAL enhances the frequency of folding in
 584 the models but leaves their width reasonably unchanged. The modeled fold amplitudes
 585 of 300-500 km are moderately smaller than the 400-700 km wide “slab walls” imaged by
 586 seismic tomography (e. g. Sigloch & Mihalynuk, 2013). It remains to be investigated
 587 whether this difference is due to shortcomings of the physical approximations used in our
 588 dynamic models, or due to tomographic blur.

589 From models of subduction dynamics, it has been suggested that sustained, quasi-
 590 periodic slab folding, over tens of millions of years after initial slab-660 interaction, can
 591 occur only if the mineralogical phase transition around 410 and 660 km were included in
 592 the models Běhounková & Čížková (2008); Čížková & Bina (2013); Agrusta et al. (2017);
 593 Briaud et al. (2020), and/or if the subducting slab was quite weak, e.g., made of young

594 seafloor Garel et al. (2014); Agrusta et al. (2017); Strak & Schellart (2021). While we
595 acknowledge that these factors may further enhance slab folding, we stress that our sim-
596 ulations with a WAL did not require the phase transitions in order to produce sustained
597 slab folding. The Clapeyron slopes of the phase transitions remain under discussion ?see
598 e.g.>[and references therein]agrusta2017subducting, so their relative role in slab folding
599 remains to be clarified. In a similar vein, the inclusion of a WAL yielded slab folding
600 of relatively thick and stiff subducting plates (Fig.12). No additional slab-weakening
601 mechanism or slab-buoyancy variation was required. We note that it has also been sug-
602 gested that vertical piles of lower-mantle slabs could only be produced in the context of
603 a fixed overriding plate Lee & King (2011); Běhouňková & Čížková (2008); Čížková &
604 Bina (2013); Billen & Arredondo (2018). Here we have demonstrated that vertical slab
605 folding slab can also occur in simulations with a WAL, in which trench retreat remains
606 self-consistently limited (Fig. 8).

607 Conclusion

608 Previous numerical and analogue models of subduction dynamics tend to produce surface
609 kinematics and lower-mantle slab morphologies that do not match first-order observa-
610 tional constraints. We have shown that including a weak asthenospheric layer below the
611 lithosphere into numerical models of subduction dynamics eliminates these mismatches.
612 The lubricating effect of the asthenosphere produces a velocity increase of the subducting
613 plate and a reduction of trench retreat, yielding predicted velocities that closely match
614 those recorded on Earth. These velocity changes are sustained long after the subducting
615 slab has penetrated into the lower mantle. The surplus of rapidly subducting lithosphere
616 is accommodated by folding, rather than by accelerating trench retreat or slab sinking.
617 This leads to an apparent horizontal widening of the slab in the lower mantle, as is ob-
618 served by seismic tomography. Substantial near-vertical slab piles accumulate over time
619 because trench motion is limited. We find that a viscosity reduction below the plate by
620 a factor of only 2 to 5 is sufficient to completely shift the dynamics in these models –
621 from non-folding with slow subduction and substantial trench retreat, to regimes of mul-
622 tiply folded, wall-like slab piles under near-stationary trenches. The latter then dominate
623 across a wide parameter space of subducting and overriding plate ages. Our results pro-
624 vide strong independent support for the presence of a weak asthenospheric layer beneath
625 Earth’s lithosphere.

References

- 626
- 627 Agrusta, R., Goes, S., & van Hunen, J. 2017, Subducting-slab transition-
628 zone interaction: Stagnation, penetration and mode switches. *Earth and*
629 *Planetary Science Letters*, 464:10–23. doi: 10.1016/j.epsl.2017.02.005. URL
630 <https://doi.org/10.1016/j.epsl.2017.02.005>.
- 631 Alsaiif, M., Garel, F., Gueydan, F., & Davies, D. R. 2020, Upper plate deformation and
632 trench retreat modulated by subduction-driven shallow asthenospheric flows. *Earth and*
633 *Planetary Science Letters*, 532:116013.
- 634 Amaru, M. *Global travel time tomography with 3-D reference models*, volume 274. Utrecht
635 University, 2007.
- 636 Arcay, D., Lallemand, S., & Doin, M.-P. 2008, Back-arc strain in subduction zones: Statis-
637 tical observations versus numerical modeling. *Geochemistry, Geophysics, Geosystems*,
638 9(5).
- 639 Argus, D. F., Gordon, R. G., & DeMets, C. 2011, Geologically current motion of 56 plates
640 relative to the no-net-rotation reference frame. *Geochemistry, Geophysics, Geosystems*,
641 12(11). doi: 10.1029/2011GC003751. URL <https://doi.org/10.1029/2011GC003751>.
- 642 Ballmer, M. D., Ito, G., Van Hunen, J., & Tackley, P. J. 2011, Spatial and temporal
643 variability in hawaiian hotspot volcanism induced by small-scale convection. *Nature*
644 *Geoscience*, 4(7):457–460.
- 645 Barruol, G., Sigloch, K., Scholz, J.-R., Mazzullo, A., Stutzmann, E., Mon-
646 tagner, J.-P., Kiselev, S., Fontaine, F. R., Michon, L., Deplus, C., et al.
647 2019, Large-scale flow of indian ocean asthenosphere driven by réunion plume.
648 *Nature Geoscience*, 12(12):1043–1049. doi: 10.1038/s41561-019-0479-3. URL
649 <https://doi.org/10.1038/s41561-019-0479-3>.
- 650 Becker, T. W. 2017, Superweak asthenosphere in light of upper mantle seismic anisotropy.
651 *Geochemistry, Geophysics, Geosystems*, 18(5):1986–2003. doi: 10.1002/2017GC006886.
652 URL <https://doi.org/10.1002/2017GC006886>.
- 653 Becker, T. W. & Faccenna, C. A review of the role of subduction dynamics for regional
654 and global plate motions. In *Subduction Zone Geodynamics*, pages 3–34. Springer, 2009.
- 655 Becker, T. W., Schaeffer, A. J., Lebedev, S., & Conrad, C. P. 2015, Toward a generalized
656 plate motion reference frame. *Geophysical Research Letters*, 42(9):3188–3196. doi:
657 10.1002/2015GL063695. URL <https://doi.org/10.1002/2015GL063695>.
- 658 Běhounková, M. & Čížková, H. 2008, Long-wavelength character of subducted slabs
659 in the lower mantle. *Earth and Planetary Science Letters*, 275(1-2):43–53. doi:
660 10.1016/j.epsl.2008.07.059. URL <https://doi.org/10.1016/j.epsl.2008.07.059>.
- 661 Behr, W. M. & Becker, T. W. 2018, Sediment control on subduction plate speeds. *Earth*
662 *and Planetary Science Letters*, 502:166–173. doi: 10.1016/j.epsl.2018.08.057. URL
663 <https://doi.org/10.1016/j.epsl.2018.08.057>.

- 664 Behr, W. M., Holt, A. F., Becker, T. W., & Faccenna, C. 2022, The effects of plate
665 interface rheology on subduction kinematics and dynamics. *Geophysical Journal Inter-*
666 *national*. doi: 10.1093/gji/ggac075. URL <https://doi.org/10.1093/gji/ggac075>.
- 667 Billen, M. I. 2010, Slab dynamics in the transition zone. *Physics of the Earth*
668 *and planetary interiors*, 183(1-2):296–308. doi: 10.1016/j.pepi.2010.05.005. URL
669 <https://doi.org/10.1016/j.pepi.2010.05.005>.
- 670 Billen, M. I. & Arredondo, K. M. 2018, Decoupling of plate-asthenosphere motion
671 caused by non-linear viscosity during slab folding in the transition zone. *Physics of*
672 *the Earth and Planetary Interiors*, 281:17–30. doi: 10.1016/j.pepi.2018.04.011. URL
673 <https://doi.org/10.1016/j.pepi.2018.04.011>.
- 674 Briaud, A., Agrusta, R., Faccenna, C., Funiciello, F., & van Hunen, J. 2020,
675 Topographic fingerprint of deep mantle subduction. *Journal of Geophysical Re-*
676 *search: Solid Earth*, 125(1):e2019JB017962. doi: 10.1029/2019JB017962. URL
677 <https://doi.org/10.1029/2019JB017962>.
- 678 Capitanio, F., Morra, G., & Goes, S. 2007, Dynamic models of downgoing plate-buoyancy
679 driven subduction: Subduction motions and energy dissipation. *Earth and Planetary*
680 *Science Letters*, 262(1):284–297. doi: 10.1016/j.epsl.2007.07.039.
- 681 Carluccio, R., Kaus, B., Capitanio, F. A., & Moresi, L. 2019, The impact of
682 a very weak and thin upper asthenosphere on subduction motions. *Geophys-*
683 *ical Research Letters*, 46(21):11893–11905. doi: 10.1029/2019GL085212. URL
684 <https://doi.org/10.1029/2019GL085212>.
- 685 Cerpa, N. G., Hassani, R., Gerbault, M., & Prévost, J.-H. 2014, A fictitious domain
686 method for lithosphere-asthenosphere interaction: Application to periodic slab folding
687 in the upper mantle. *Geochemistry, Geophysics, Geosystems*, 15(5):1852–1877. doi:
688 10.1002/2014GC005241. URL <https://doi.org/10.1002/2014GC005241>.
- 689 Cerpa, N. G., Araya, R., Gerbault, M., & Hassani, R. 2015, Relationship be-
690 tween slab dip and topography segmentation in an oblique subduction zone: In-
691 sights from numerical modeling. *Geophysical Research Letters*, 42(14):5786–5795. doi:
692 10.1002/2015GL064047.
- 693 Cerpa, N. G., Guillaume, B., & Martinod, J. 2018, The interplay between overriding
694 plate kinematics, slab dip and tectonics. *Geophysical Journal International*, 215(3):
695 1789–1802. doi: 10.1093/gji/ggy365.
- 696 Chantel, J., Manthilake, G., Andrault, D., Novella, D., Yu, T., & Wang, Y. 2016, Ex-
697 perimental evidence supports mantle partial melting in the asthenosphere. *Science*
698 *advances*, 2(5):e1600246. URL <https://doi.org/10.1126/sciadv.1600246>.
- 699 Christensen, U. R. 1996, The influence of trench migration on slab penetration into the
700 lower mantle. *Earth and Planetary Science Letters*, 140(1):27–39. doi: 10.1016/0012-
701 821X(96)00023-4.
- 702 Čížková, H. & Bina, C. 2013, Effects of mantle and subduction-interface rheologies on
703 slab stagnation and trench rollback. *Earth and Planetary Science Letters*, 379:95–103.
704 doi: 10.1016/j.epsl.2013.08.011.

- 705 Čížková, H. & Bina, C. R. 2015, Geodynamics of trench advance: Insights from a
706 philippine-sea-style geometry. *Earth and Planetary Science Letters*, 430:408–415. doi:
707 10.1016/j.epsl.2015.07.004. URL <https://doi.org/10.1016/j.epsl.2015.07.004>.
- 708 Čížková, H., van den Berg, A. P., Spakman, W., & Matyska, C. 2012, The viscosity of
709 earth’s lower mantle inferred from sinking speed of subducted lithosphere. *Physics of
710 the earth and Planetary Interiors*, 200:56–62. doi: 10.1016/j.pepi.2012.02.010. URL
711 <https://doi.org/10.1016/j.pepi.2012.02.010>.
- 712 Coltice, N., Rolf, T., Tackley, P. J., & Labrosse, S. 2012, Dynamic causes of the relation
713 between area and age of the ocean floor. *Science*, 336(6079):335–338. doi: 10.1126/sci-
714 ence.1219120. URL <https://doi.org/10.1126/science.1219120>.
- 715 Conrad, C. P. & Behn, M. D. 2010, Constraints on lithosphere net rotation and as-
716 thenospheric viscosity from global mantle flow models and seismic anisotropy. *Geo-
717 chemistry, Geophysics, Geosystems*, 11(5). doi: 10.1029/2009GC002970. URL
718 <https://doi.org/10.1029/2009GC002970>.
- 719 Cooper, R. & Kohlstedt, D. 1986, Rheology and structure of olivine-basalt par-
720 tial melts. *Journal of Geophysical Research: Solid Earth*, 91(B9):9315–9323. doi:
721 10.1029/JB091iB09p09315. URL <https://doi.org/10.1029/JB091iB09p09315>.
- 722 Davies, D. R., Wilson, C., & Kramer, S. 2011, Fluidity: A fully unstructured
723 anisotropic adaptive mesh computational modeling framework for geodynamics. *Geo-
724 chemistry, Geophysics, Geosystems*, 12(6). doi: 10.1029/2011GC003551. URL
725 <https://doi.org/10.1029/2011GC003551>.
- 726 Davies, D. R., Le Voci, G., Goes, S., Kramer, S. C., & Wilson, C. R. 2016, The mantle
727 wedge’s transient 3-D flow regime and thermal structure. *Geochem. Geophys. Geosys.*,
728 17:78–100. doi: 10.1002/2015GC006125.
- 729 Davies, G. 1981, Regional compensation of subducted lithosphere: effects on
730 geoid, gravity and topography from a preliminary model. *Earth and Plane-
731 tary Science Letters*, 54(3):431–441. doi: 10.1016/0012-821X(81)90059-5. URL
732 [https://doi.org/10.1016/0012-821X\(81\)90059-5](https://doi.org/10.1016/0012-821X(81)90059-5).
- 733 Debayle, E., Bodin, T., Durand, S., & Ricard, Y. 2020, Seismic evidence for partial melt
734 below tectonic plates. *Nature*, 586(7830):555–559. doi: 10.1038/s41586-020-2809-4.
735 URL <https://doi.org/10.1038/s41586-020-2809-4>.
- 736 Debayle, E. & Ricard, Y. 2013, Seismic observations of large-scale deformation at the
737 bottom of fast-moving plates. *Earth and Planetary Science Letters*, 376:165–177. doi:
738 10.1016/j.epsl.2013.06.025. URL <https://doi.org/10.1016/j.epsl.2013.06.025>.
- 739 Di Giuseppe, E., Van Hunen, J., Funiciello, F., Faccenna, C., & Giardini, D. 2008,
740 Slab stiffness control of trench motion: Insights from numerical models. *Geochemistry,
741 Geophysics, Geosystems*, 9(2).
- 742 Doglioni, C., Carminati, E., Cuffaro, M., & Scrocca, D. 2007, Subduction kinematics and
743 dynamic constraints. *Earth-Science Reviews*, 83(3):125–175.

- 744 Domeier, M., Doubrovine, P. V., Torsvik, T. H., Spakman, W., & Bull, A. L.
745 2016, Global correlation of lower mantle structure and past subduction. *Geo-*
746 *physical Research Letters*, 43(10):4945–4953. doi: 10.1002/2016GL068827. URL
747 <https://doi.org/10.1002/2016GL068827>.
- 748 Doubrovine, P. V., Steinberger, B., & Torsvik, T. H. 2012, Absolute plate motions in a
749 reference frame defined by moving hot spots in the pacific, atlantic, and indian oceans.
750 *Journal of Geophysical Research: Solid Earth*, 117(B9). doi: 10.1029/2011JB009072.
751 URL <https://doi.org/10.1029/2011JB009072>.
- 752 Forsyth, D. & Uyeda, S. 1975, On the relative importance of the driving forces of plate
753 motion. *Geophysical Journal International*, 43(1):163–200.
- 754 French, S., Lekic, V., & Romanowicz, B. 2013, Waveform tomography reveals chan-
755 nelled flow at the base of the oceanic asthenosphere. *Science*, 342(6155):227–230. doi:
756 10.1126/science.1241514. URL <https://doi.org/10.1126/science.1241514>.
- 757 Fukao, Y. & Obayashi, M. 2013, Subducted slabs stagnant above, penetrating through,
758 and trapped below the 660 km discontinuity. *Journal of Geophysical Research: Solid*
759 *Earth*, 118(11):5920–5938. doi: 10.1002/2013JB010466.
- 760 Fukao, Y., Obayashi, M., Inoue, H., & Nenbai, M. 1992, Subducting slabs stagnant in
761 the mantle transition zone. *Journal of Geophysical Research: Solid Earth (1978–2012)*,
762 97(B4):4809–4822.
- 763 Funiciello, F., Faccenna, C., & Giardini, D. 2004, Role of lateral mantle flow in the
764 evolution of subduction systems: insights from laboratory experiments. *Geophysical*
765 *Journal International*, 157(3):1393–1406. doi: 10.1111/j.1365-246X.2004.02313.x.
- 766 Funiciello, F., Faccenna, C., Heuret, A., Lallemand, S., Di Giuseppe, E., & Becker, T.
767 2008, Trench migration, net rotation and slab–mantle coupling. *Earth and Planetary*
768 *Science Letters*, 271(1):233–240. doi: 10.1016/j.epsl.2008.04.006.
- 769 Garel, F., Goes, S., Davies, D. R., Davies, J., Kramer, S., & Wilson, C. 2014,
770 Interaction of subducted slabs with the mantle transition-zone: A regime dia-
771 gram from 2-d thermo-mechanical models with a mobile trench and an overriding
772 plate. *Geochemistry, Geophysics, Geosystems*. doi: 10.1002/2014GC005257. URL
773 <https://doi.org/10.1002/2014GC005257>.
- 774 Garel, F., Thoraval, C., Tommasi, A., Demouchy, S., & Davies, D. R. 2020, Using
775 thermo-mechanical models of subduction to constrain effective mantle viscosity. *Earth*
776 *and Planetary Science Letters*, 539:116243.
- 777 Gibert, G., Gerbault, M., Hassani, R., & Tric, E. 2012, Dependency of slab geometry on
778 absolute velocities and conditions for cyclicity: insights from numerical modelling. *Geo-*
779 *physical Journal International*, 189(2):747–760. ISSN 1365-246X. doi: 10.1111/j.1365-
780 246X.2012.05426.x. URL <https://doi.org/10.1111/j.1365-246X.2012.05426.x>.
- 781 Goes, S., Capitanio, F. A., Morra, G., Seton, M., & Giardini, D. 2011, Signatures of
782 downgoing plate-buoyancy driven subduction in cenozoic plate motions. *Physics of*
783 *the Earth and Planetary Interiors*, 184(1):1–13. doi: 10.1016/j.pepi.2010.10.007. URL
784 <https://doi.org/10.1016/j.pepi.2010.10.007>.

- 785 Goes, S., Agrusta, R., Van Hunen, J., & Garel, F. 2017, Subduction-transition zone
786 interaction: A review. *Geosphere*, 13(3):644–664. doi: 10.1130/GES01476.1. URL
787 <https://doi.org/10.1130/GES01476.1>.
- 788 Guillaume, B., Hertgen, S., Martinod, J., & Cerpa, N. 2018, Slab dip, surface tectonics:
789 How and when do they change following an acceleration/slow down of the overriding
790 plate? *Tectonophysics*, 726:110–120. doi: 10.1016/j.tecto.2018.01.030.
- 791 Guillou-Frottier, L., Buttles, J., & Olson, P. 1995, Laboratory experiments on the struc-
792 ture of subducted lithosphere. *Earth and Planetary Science Letters*, 133(1):19–34.
- 793 Gurnis, M. 1993, Phanerozoic marine inundation of continents driven by dynamic to-
794 pography above subducting slabs. *Nature*, 364(6438):589–593. doi: 10.1038/364589a0.
795 URL <https://doi.org/10.1038/364589a0>.
- 796 Hertgen, S., Yamato, P., Guillaume, B., Magni, V., Schliffke, N., & van Hunen, J. 2020, In-
797 fluence of the thickness of the overriding plate on convergence zone dynamics. *Geochem-
798 istry, Geophysics, Geosystems*, 21(2):e2019GC008678. doi: 10.1029/2019GC008678.
799 URL <https://doi.org/10.1029/2019GC008678>.
- 800 Heuret, A. & Lallemand, S. 2005, Plate motions, slab dynamics and back-arc
801 deformation. *Physics of the Earth and Planetary Interiors*, 149(1):31–51. doi:
802 10.1016/j.pepi.2004.08.022.
- 803 Heuret, A., Funicello, F., Faccenna, C., & Lallemand, S. 2007, Plate kinematics,
804 slab shape and back-arc stress: a comparison between laboratory models and cur-
805 rent subduction zones. *Earth and Planetary Science Letters*, 256(3):473–483. doi:
806 10.1016/j.epsl.2007.02.004.
- 807 Höink, T., Lenardic, A., & Richards, M. 2012, Depth-dependent viscosity and man-
808 tle stress amplification: implications for the role of the asthenosphere in maintaining
809 plate tectonics. *Geophysical Journal International*, 191(1):30–41. doi: 10.1111/j.1365-
810 246X.2012.05621.x. URL <https://doi.org/10.1111/j.1365-246X.2012.05621.x>.
- 811 Holt, A., Becker, T., & Buffett, B. 2015, Trench migration and overriding plate stress in
812 dynamic subduction models. *Geophysical Journal International*, 201(1):172–192. doi:
813 10.1093/gji/ggv011. URL <https://doi.org/10.1093/gji/ggv011>.
- 814 Holtzman, B. K. 2016, Questions on the existence, persistence, and mechani-
815 cal effects of a very small melt fraction in the asthenosphere. *Geochemistry,
816 Geophysics, Geosystems*, 17(2):470–484. doi: 10.1002/2015GC006102. URL
817 <https://doi.org/10.1002/2015GC006102>.
- 818 Hosseini, K., Sigloch, K., Tsekhmistrenko, M., Zaheri, A., Nissen-Meyer, T., & Igel,
819 H. 2020, Global mantle structure from multifrequency tomography using p, pp
820 and p-diffracted waves. *Geophysical Journal International*, 220(1):96–141. doi:
821 10.1093/gji/ggz394. URL <https://doi.org/10.1093/gji/ggz394>.
- 822 Jarrard, R. D. 1986, Relations among subduction parameters. *Reviews of Geophysics*, 24
823 (2):217–284. doi: 10.1029/RG024i002p00217.

- 824 Jones, T., Davies, D., Campbell, I., Wilson, C., & Kramer, S. 2016, Do mantle plumes
825 preserve the heterogeneous structure of their deep-mantle source? *Earth Planet. Sci.*
826 *Lett.*, 434:10 – 17. doi: 10.1016/j.epsl.2015.11.016.
- 827 Karason, H. & Van Der Hilst, R. D. 2000, Constraints on mantle convection from seismic
828 tomography. *The History and Dynamics of Global Plate Motions*, pages 277–288.
- 829 Kawakatsu, H., Kumar, P., Takei, Y., Shinohara, M., Kanazawa, T., Araki, E., &
830 Suyehiro, K. 2009, Seismic evidence for sharp lithosphere-asthenosphere boundaries
831 of oceanic plates. *science*, 324(5926):499–502. doi: 10.1126/science.1169499. URL
832 <https://doi.org/10.1126/science.1169499>.
- 833 Kohlstedt, D. L. & Zimmerman, M. E. 1996, Rheology of partially molten mantle
834 rocks. *Annual Review of Earth and Planetary Sciences*, 24(1):41–62. doi: 10.1146/an-
835 nurev.earth.24.1.41. URL <https://doi.org/10.1146/annurev.earth.24.1.41>.
- 836 Kramer, S., Wilson, C., & Davies, D. R. 2012, An implicit free surface algorithm for
837 geodynamical simulations. *Physics of the Earth and Planetary Interiors*, 194:25–37. doi:
838 10.1016/j.pepi.2012.01.001. URL <https://doi.org/10.1016/j.pepi.2012.01.001>.
- 839 Kramer, S. C., Davies, D. R., & Wilson, C. R. 2021, Analytical solutions for mantle flow in
840 cylindrical and spherical shells. *Geosci. Model Dev.*, 14:1899–1919. doi: 10.5194/gmd-
841 14-1899-2021.
- 842 Lallemand, S., Heuret, A., & Boutelier, D. 2005, On the relationships between slab dip,
843 back-arc stress, upper plate absolute motion, and crustal nature in subduction zones.
844 *Geochemistry, Geophysics, Geosystems*, 6(9). doi: 10.1029/2005GC000917.
- 845 Le Voci, G., Davies, D. R., Goes, S., Kramer, S. C., & Wilson, C. R. 2014, A systematic
846 2-D investigation into the mantle wedge’s transient flow regime and thermal structure:
847 complexities arising from a hydrated rheology and thermal buoyancy. *Geochem. Geo-*
848 *phys. Geosys.*, 15:28–51. doi: 10.1002/2013GC005022.
- 849 Lee, C. & King, S. D. 2011, Dynamic buckling of subducting slabs reconciles geological
850 and geophysical observations. *Earth and Planetary Science Letters*, 312(3):360–370.
- 851 Lenardic, A., Richards, M., & Busse, F. H. 2006, Depth-dependent rheology and the
852 horizontal length scale of mantle convection. *Journal of Geophysical Research: Solid*
853 *Earth*, 111(B7).
- 854 Li, C., van der Hilst, R. D., Engdahl, E. R., & Burdick, S. 2008, A new global model for
855 p wave speed variations in earth’s mantle. *Geochemistry, Geophysics, Geosystems*, 9
856 (5).
- 857 Li, Z.-H., Gerya, T., & Connolly, J. A. 2019, Variability of subducting slab morpholo-
858 gies in the mantle transition zone: Insight from petrological-thermomechanical mod-
859 eling. *Earth-Science Reviews*, 196:102874. doi: 10.1016/j.earscirev.2019.05.018. URL
860 <https://doi.org/10.1016/j.earscirev.2019.05.018>.
- 861 Loiselet, C., Braun, J., Husson, L., Le Carlier de Veslud, C., Thieulot, C., Yam-
862 ato, P., & Grujic, D. 2010, Subducting slabs: Jellyfishes in the earth’s mantle.
863 *Geochemistry, Geophysics, Geosystems*, 11(8). doi: 10.1029/2010GC003172. URL
864 <https://doi.org/10.1029/2010GC003172>.

- 865 Lyu, T., Zhu, Z., & Wu, B. 2019, Subducting slab morphology and mantle transi-
866 tion zone upwelling in double-slab subduction models with inward-dipping directions.
867 *Geophysical Journal International*, 218(3):2089–2105. doi: 10.1093/gji/ggz268. URL
868 <https://doi.org/10.1093/gji/ggz268>.
- 869 Meyers, C. D. & Kohlstedt, D. L. 2021, Experimental measurements
870 of anisotropic viscosity in naturally sourced dunite with a preexisting
871 cpo. *Tectonophysics*, 815:228949. doi: 10.1016/j.tecto.2021.228949. URL
872 <https://doi.org/10.1016/j.tecto.2021.228949>.
- 873 Mitrovica, J. & Forte, A. 2004, A new inference of mantle viscosity based upon joint
874 inversion of convection and glacial isostatic adjustment data. *Earth and Planetary
875 Science Letters*, 225(1):177–189. doi: 10.1016/j.epsl.2004.06.005.
- 876 Mohammadzaheri, A., Sigloch, K., Hosseini, K., & Mihalynuk, M. G. 2021, Subducted
877 lithosphere under south america from multi-frequency p-wave tomography. *Journal of
878 Geophysical Research: Solid Earth*, 126:e2020JB020704. doi: 10.1029/2020JB020704.
879 URL <https://doi.org/10.1029/2020JB020704>.
- 880 Naif, S., Key, K., Constable, S., & Evans, R. 2013, Melt-rich channel observed at the
881 lithosphere–asthenosphere boundary. *Nature*, 495(7441):356–359. doi: 10.1038/nature11939. URL <https://doi.org/10.1038/nature11939>.
- 883 Paulson, A. & Richards, M. A. 2009, On the resolution of radial viscosity struc-
884 ture in modelling long-wavelength postglacial rebound data. *Geophysical Jour-
885 nal International*, 179(3):1516–1526. doi: 10.1111/j.1365-246X.2009.04362.x. URL
886 <https://doi.org/10.1111/j.1365-246X.2009.04362.x>.
- 887 Phipps Morgan, J., Morgan, W. J., Zhang, Y.-S., & Smith, W. H. 1995, Observa-
888 tional hints for a plume-fed, suboceanic asthenosphere and its role in mantle con-
889 vection. *Journal of Geophysical Research: Solid Earth*, 100(B7):12753–12767. doi:
890 10.1029/95JB00041. URL <https://doi.org/10.1029/95JB00041>.
- 891 Pusok, A. E., Stegman, D. R., & Kerr, M. PREPRINT, The effect of sediments on the
892 dynamics and accretionary style of subduction margins. *Solid Earth Discussions*, pages
893 1–30.
- 894 Raterron, P., Chen, J., Geenen, T., & Girard, J. 2011, Pressure effect on forsterite
895 dislocation slip systems: Implications for upper-mantle lpo and low viscosity zone.
896 *Physics of the Earth and Planetary Interiors*, 188(1-2):26–36.
- 897 Ren, Y., Stutzmann, E., van Der Hilst, R. D., & Besse, J. 2007, Understanding seismic
898 heterogeneities in the lower mantle beneath the americas from seismic tomography and
899 plate tectonic history. *Journal of Geophysical Research: Solid Earth*, 112(B1). doi:
900 10.1029/2005JB004154. URL <https://doi.org/10.1029/2005JB004154>.
- 901 Ribe, N. M. 2003, Periodic folding of viscous sheets. *Physical Review E*, 68(3):036305.
902 doi: 10.1103/PhysRevE.68.036305.
- 903 Ribe, N. M. 2010, Bending mechanics and mode selection in free subduction: a thin-
904 sheet analysis. *Geophysical Journal International*, 180(2):559–576. doi: 10.1111/j.1365-
905 246X.2009.04460.x. URL <https://doi.org/10.1111/j.1365-246X.2009.04460.x>.

- 906 Ribe, N. M., Stutzmann, E., Ren, Y., & Van Der Hilst, R. 2007, Buckling instabilities
907 of subducted lithosphere beneath the transition zone. *Earth and Planetary Science*
908 *Letters*, 254(1):173–179.
- 909 Sakamaki, T., Suzuki, A., Ohtani, E., Terasaki, H., Urakawa, S., Katayama, Y., Fu-
910 nakoshi, K.-i., Wang, Y., Hernlund, J. W., & Ballmer, M. D. 2013, Ponded melt at
911 the boundary between the lithosphere and asthenosphere. *Nature Geoscience*, 6(12):
912 1041–1044. doi: 10.1038/ngeo1982. URL <https://doi.org/10.1038/ngeo1982>.
- 913 Schellart, W. P. 2008a, Kinematics and flow patterns in deep mantle and upper mantle
914 subduction models: Influence of the mantle depth and slab to mantle viscosity ra-
915 tio. *Geochemistry, Geophysics, Geosystems*, 9(3). doi: 10.1029/2004JB002970. URL
916 <https://doi.org/10.1111/10.1029/2004JB002970>.
- 917 Schellart, W. P. 2008b, Subduction zone trench migration: Slab driven or overriding-
918 plate-driven? *Physics of the Earth and Planetary Interiors*, 170(1-2):73–88. doi:
919 10.1016/j.pepi.2008.07.040. URL <https://doi.org/10.1016/j.pepi.2008.07.040>.
- 920 Schellart, W. P. 2005, Influence of the subducting plate velocity on the ge-
921 ometry of the slab and migration of the subduction hinge. *Earth and Plan-*
922 *etary Science Letters*, 231(3-4):197–219. doi: 10.1016/j.epsl.2004.12.019. URL
923 <https://doi.org/10.1016/j.epsl.2004.12.019>.
- 924 Schmerr, N. 2012, The gutenbergs discontinuity: Melt at the lithosphere-asthenosphere
925 boundary. *Science*, 335(6075):1480–1483. doi: 10.1126/science.1215433. URL
926 <https://doi.org/10.1126/science.1215433>.
- 927 Sdrolias, M. & Müller, R. 2006, Controls on back-arc basin formation. *Geochemistry,*
928 *Geophysics, Geosystems*, 7(4). doi: 10.1029/2005GC001090.
- 929 Sharples, W., Jadamec, M., Moresi, L., & Capitanio, F. 2014, Overriding plate controls on
930 subduction evolution. *Journal of Geophysical Research: Solid Earth*, 119(8):6684–6704.
931 doi: 10.1002/2014JB011163. URL <https://doi.org/10.1002/2014JB011163>.
- 932 Shephard, G. E., Matthews, K. J., Hosseini, K., & Domeier, M. 2017, On the con-
933 sistency of seismically imaged lower mantle slabs. *Scientific reports*, 7(1):1–17. doi:
934 10.1038/s41598-017-11039-w. URL <https://doi.org/10.1038/s41598-017-11039-w>.
- 935 Sigloch, K. & Mihalynuk, M. G. 2013, Intra-oceanic subduction shaped the assembly of
936 cordilleran north america. *Nature*, 496(7443):50–56. doi: 10.1038/nature12019. URL
937 <https://doi.org/10.1038/nature12019>.
- 938 Sigloch, K., McQuarrie, N., & Nolet, G. 2008, Two-stage subduction history under north
939 america inferred from multiple-frequency tomography. *Nature Geoscience*, 1(7):458–
940 462.
- 941 Stegman, D., Farrington, R., Capitanio, F. A., & Schellart, W. P. 2010, A
942 regime diagram for subduction styles from 3-d numerical models of free sub-
943 duction. *Tectonophysics*, 483(1):29–45. doi: 10.1016/j.tecto.2009.08.041. URL
944 <https://doi.org/10.1016/j.tecto.2009.08.041>.

- 945 Stern, T., Henrys, S. A., Okaya, D., Louie, J. N., Savage, M. K., Lamb, S., Sato,
946 H., Sutherland, R., & Iwasaki, T. 2015, A seismic reflection image for the base
947 of a tectonic plate. *Nature*, 518(7537):85–88. doi: 10.1038/nature14146. URL
948 <https://doi.org/10.1038/nature14146>.
- 949 Strak, V. & Schellart, W. 2021, Thermo-mechanical numerical modeling of the south
950 american subduction zone: A multi-parametric investigation. *Journal of Geophysi-
951 cal Research: Solid Earth*, 126(4):e2020JB021527. doi: 10.1029/2020JB021527. URL
952 <https://doi.org/10.1029/2020JB021527>.
- 953 Suchoy, L., Goes, S., Maunder, B., Garel, F., & Davies, D. R. 2021, Effects of basal
954 drag on subduction dynamics from 2d numerical models. *Solid Earth*, 12(1):79–93. doi:
955 10.5194/se-12-79-2021. URL <https://doi.org/10.5194/se-12-79-2021>.
- 956 Torii, Y. & Yoshioka, S. 2007, Physical conditions producing slab stagnation:
957 Constraints of the clapeyron slope, mantle viscosity, trench retreat, and dip an-
958 gles. *Tectonophysics*, 445(3):200–209. doi: 10.1016/j.tecto.2007.08.003. URL
959 <https://doi.org/10.1016/j.tecto.2007.08.003>.
- 960 Uyeda, S. & Kanamori, H. 1979, Back-arc opening and the mode of subduction.
961 *Journal of Geophysical Research: Solid Earth (1978–2012)*, 84(B3):1049–1061. doi:
962 10.1029/JB084iB03p01049. URL <https://doi.org/10.1029/JB084iB03p01049>.
- 963 Van Der Meer, D. G., Spakman, W., Van Hinsbergen, D. J., Amaru, M. L., &
964 Torsvik, T. H. 2010, Towards absolute plate motions constrained by lower-mantle
965 slab remnants. *Nature Geoscience*, 3(1):36–40. doi: 10.1038/ngeo708. URL
966 <https://doi.org/10.1038/ngeo708>.
- 967 Van der Meer, D. G., Van Hinsbergen, D. J., & Spakman, W. 2018, Atlas of the under-
968 world: Slab remnants in the mantle, their sinking history, and a new outlook on lower
969 mantle viscosity. *Tectonophysics*, 723:309–448. doi: 10.1016/j.tecto.2017.10.004. URL
970 <https://doi.org/10.1016/j.tecto.2017.10.004>.
- 971 Van der Voo, R., Spakman, W., & Bijwaard, H. 1999, Tethyan subducted slabs un-
972 der india. *Earth and Planetary Science Letters*, 171(1):7–20. doi: 10.1016/S0012-
973 821X(99)00131-4. URL [https://doi.org/10.1016/S0012-821X\(99\)00131-4](https://doi.org/10.1016/S0012-821X(99)00131-4).
- 974 van Hunen, J., Huang, J., & Zhong, S. 2003, The effect of shearing on the onset and vigor
975 of small-scale convection in a newtonian rheology. *Geophysical research letters*, 30(19).
- 976 Wang, S., Yu, H., Zhang, Q., & Zhao, Y. 2018, Absolute plate motions relative
977 to deep mantle plumes. *Earth and Planetary Science Letters*, 490:88–99. doi:
978 10.1016/j.epsl.2018.03.021. URL <https://doi.org/10.1016/j.epsl.2018.03.021>.
- 979 Wu, J., Suppe, J., Lu, R., & Kanda, R. 2016, Philippine sea and east asian plate tectonics
980 since 52 ma constrained by new subducted slab reconstruction methods. *Journal of
981 Geophysical Research: Solid Earth*, 121(6):4670–4741. doi: 10.1002/2016JB012923.
982 URL <https://doi.org/10.1002/2016JB012923>.
- 983 Zhang, H., Wang, F., Myhill, R., & Guo, H. 2019, Slab morphology and deformation
984 beneath izu-bonin. *Nature communications*, 10(1):1–8. doi: 10.1038/s41467-019-09279-
985 7. URL <https://doi.org/10.1038/s41467-019-09279-7>.

986 Zindler, A. & Hart, S. 1986, Chemical geodynamics. *Annual review of earth and*
987 *planetary sciences*, 14(1):493–571. doi: 10.1146/annurev.ea.14.050186.002425. URL
988 <https://doi.org/10.1146/annurev.ea.14.050186.002425>.